Introducing Quantum Ricci Curvature

N. Klitgaard[a] and *R. Loll*[a,b]

[a] Institute for Mathematics, Astrophysics and Particle Physics, Radboud University
Heyendaalseweg 135, 6525 AJ Nijmegen, The Netherlands.
email: n.klitgaard@science.ru.nl, r.loll@science.ru.nl

[b] Perimeter Institute for Theoretical Physics,
31 Caroline St N, Waterloo, Ontario N2L 2Y5, Canada.
email: rloll@perimeterinstitute.ca

Abstract

Motivated by the search for geometric observables in nonperturbative quantum gravity, we define a notion of coarse-grained Ricci curvature. It is based on a particular way of extracting the local Ricci curvature of a smooth Riemannian manifold by comparing the distance between pairs of spheres with that of their centres. The quantum Ricci curvature is designed for use on non-smooth and discrete metric spaces, and to satisfy the key criteria of scalability and computability. We test the prescription on a variety of regular and random piecewise flat spaces, mostly in two dimensions. This enables us to quantify its behaviour for short lattices distances and compare its large-scale behaviour with that of constantly curved model spaces. On the triangulated spaces considered, the quantum Ricci curvature has good averaging properties and reproduces classical characteristics on scales large compared to the discretization scale.

1 The case for quantum observables

A crucial ingredient for understanding the physics of nonperturbative quantum gravity are observables that capture the properties of spacetime in a diffeomorphism-invariant and background-independent manner, all the way down to the Planck scale. Thus far, there are very few quantities we know of that fit the bill.

The nonperturbative path-integral approach of Causal Dynamical Triangulations (CDT) has proven a fertile ground for defining and studying such observables [1]. Firstly, the manifest coordinate-invariance of the underlying piecewise flat Regge geometries (the "triangulations") makes this approach purely geometric, in keeping with the spirit of Einstein's classical theory. By contrast, quantum formulations that use a differentiable manifold or some regularized version thereof as part of their background structure usually require a choice of coordinates to do explicit computations. In this case, the implementation of a suitable gauge fixing and the consistent treatment of diffeomorphism symmetry in the quantum theory often face protracted difficulties. Secondly, CDT provides a well-defined computational framework, in which the expectation values of observables can be measured and studied systematically in the limit as the UV-cutoff – the so-called "lattice spacing" a – is removed.

This has enabled the operational definition and quantitative evaluation of several interesting observables. Among them, the spectral dimension [2] is perhaps the best known. It only requires the existence of an operator of Laplace-type and is therefore relatively straightforward to implement in a variety of ways also in other quantum gravity approaches (see [3, 4] and references therein). Measurements of the spectral dimension of the quantum geometry generated in CDT quantum gravity first exhibited the phenomenon of "dynamical dimensional reduction" of spacetime from its classical value of 4 on macroscopic scales to a value compatible with 2 on the Planck scale. Other observables used to characterize the micro- and macroscopic properties of quantum spacetime are its Hausdorff dimension and the so-called volume profile of the universe, i.e. its three-volume as a function of cosmological proper time [5]. The latter has also been investigated recently with the help of functional renormalization group techniques [6].

It would clearly be desirable to have more observables that characterize some analogue of local geometry in the Planckian regime, beyond the notions of generalized dimensions currently in use. Note that these dimensions have a number of nice properties that we may want other observables to possess also. They can be defined operationally through length and volume measurements, which do not require the presence of a smooth metric $g_{\mu\nu}(x)$, but can be performed on piecewise flat manifolds and even more general metric spaces. At the same time, they *can* also be implemented on a smooth D-dimensional metric manifold to determine its local dimension, in which case they simply reproduce the value D

of its topological dimension. In other words, the generalized dimensions possess a well-defined classical limit, which justifies calling them "dimension" in the first place, even when using them in a non-classical, non-smooth context.

Another property of the generalized dimensions is that they can be scaled, in the sense that one and the same measuring prescription can be implemented at various length scales to extract an "effective dimension" associated with that scale. For example, one may obtain a Hausdorff dimension D_H of some metric space by measuring the leading-order behaviour of the volumes $V(r)$ of geodesic balls of radius r as a function of r. The exponent D_H extracted from a power law of the form $V(r) \propto r^{D_H}$ will then in general depend on the scale r. Of course, care is required when interpreting "dimension" away from a regime where it behaves classically. Note also that by using the word "observable" we do not mean to imply any link to concrete quantum gravity phenomenology but only a quantity that is operationally well defined in a nonperturbative context. Lastly, when working in the context of dynamical triangulations, the usual logic of a "lattice" regularization[1] applies: measurements at or near the cut-off scale a are discarded because of their dependence on the details of the regularization, like the shape of the elementary building blocks. Furthermore, we are only interested in continuum properties, that is, properties that persist in the limit where the regulators are removed. Most quantities one can define on the lattice will have no continuum analogue, and will not exhibit characteristic scaling behaviour in the limit as $a \to 0$ that would allow us to identify them with dimensionful, physically interesting continuum quantities.[2]

In the present work, we will introduce a new geometric observable that has many of the desirable properties just described, a quasi-local quantity we call the "quantum Ricci curvature". It is defined in purely geometric terms, without invoking any particular coordinate system, and has a well-defined classical meaning – in fact, we will construct it first on smooth Riemannian spaces. It also scales, in the sense that the quantity we will define operationally is the "quantum Ricci curvature at a given length scale". The seed of the idea owes much to the work of Ollivier on discrete or coarse-grained Ricci curvature [7, 8]. However, we had to alter his prescription quite substantially to make it suitable for application in nonperturbative quantum gravity.

After giving a brief motivation for studying quantum implementations of cur-

---

[1] We put "lattice" in inverted commas, because the notion is potentially misleading in the context of piecewise flat spaces. In such a formulation, space(-time) itself is not a lattice, but perfectly continuous. Nevertheless, since CDT works with a small number of standardized simplicial building blocks, it is natural to measure lengths only along edges and in integer multiples of a unit edge length, as a convenient approximation.

[2] The lattice spacing a has the dimension of length. In what follows, we will for simplicity often work with dimensionless lattice units, which amounts to "setting a equal to 1".

vature in the next section, we present our explicit construction of the classical version of quantum Ricci curvature in Sec. 3. In Sec. 4 we perform a quantitative analysis of this quantity on smooth, two-dimensional, constantly curved model spaces, in order to understand that the prescription is meaningful and to establish a reference frame for the evaluation of the quantum Ricci curvature on non-smooth spaces. Since our ultimate goal is the nonperturbative quantum theory, in the formulation of CDT, we then implement our curvature construction on a variety of piecewise flat spaces. This allows us to understand the differences between continuum and discrete spaces and to quantify short-distance lattice artefacts. Several regular lattices in two and three dimensions are treated in Sec. 5, and a variety of two-dimensional, equilateral random triangulations based on Delaunay triangulations in Sec. 6. This demonstrates the computational feasibility of quantum Ricci curvature and illustrates its behaviour under spatial averaging. Our conclusions and outlook are presented in Sec. 7.

2 The case for (quantum) curvature

The key notion by which we understand and quantify the nontrivial local properties of classical spacetime is that of *curvature*. While most of our intuition about curvature comes from studying two-dimensional surfaces imbedded in three-dimensional Euclidean space, intrinsic curvature in four dimensions – as captured by the Riemann curvature tensor $R^{\kappa}{}_{\lambda\mu\nu}(x)$ – is a complex and rather unintuitive quantity. Moreover, the components of the curvature tensor are not elementary, but derived quantities, depending on the second derivatives of the metric tensor, which requires $g_{\mu\nu}(x)$ to be at least twice differentiable. In situations where the metric structure is not of this type, it is clear that the definition of curvature will in general have to be modified to remain a meaningful concept. This will also be the case for the type of "quantum geometry" we are interested in, which is obtained as a continuum limit of an ensemble of piecewise flat geometries.

We will introduce below a specific notion of coarse-grained Ricci curvature that can be used in the context of nonperturbative, background-independent quantum gravity. Like the dynamical dimensions mentioned above, the construction is in terms of measurements of volumes and distances. As a consequence, it is robust and scalable, and can be implemented in a straightforward way on piecewise flat spaces, like those of Dynamical Triangulations.

Note that we are not interested in investigating a classical limit in which a sequence of triangulated spaces approaches a given smooth, classical metric manifold, and where one can then ask whether and how a particular notion of piecewise flat curvature converges to its smooth counterpart. Instead, in the gravitational path integral one considers a whole ensemble of spacetimes, and looks for continuum limits in which relevant observables exhibit a physically interesting scaling behaviour, and where most of the details of the regularization become irrelevant.

There are already notions of curvature that have been used in this context, based on the concept of a deficit angle, a simplicial implementation of describing the sectional curvature of two-dimensional subspaces. Regge calculus works with a standard expression for the scalar curvature in terms of deficit angles [9]. Its integrated version appears in a simplicial analogue of the Einstein-Hilbert action, which is also used in quantum Regge calculus and Dynamical Triangulations [10]. In the context of Regge calculus, related simplicial representations have been constructed for more complicated curvature tensors (see, for example, [11, 12, 13]).

However, these expressions are not well suited as quantum observables in our sense. The main issue is that the underlying notion of curvature defect is defined at the cutoff scale only. It does not scale since there is no obvious way of defining a coarse-grained deficit angle. In nonperturbative quantum gravity models of the kind we are considering, integrated versions of the simplicial scalar curvature for $D > 2$ tend to be highly divergent in the continuum limit. This happens because the density of the curvature defects grows as the lattice spacing a goes to zero, while the individual deficit angles do not "average out" on coarse-grained scales. The alternative curvature observable we will define and implement in this work both scales and has a better averaging behaviour, as we will demonstrate explicitly.

The generalized notion of Ricci curvature introduced in the next section is not based on measuring deficit angles, but – in a D-dimensional space – involves the average distance between two overlapping $(D-1)$-dimensional spheres. The construction is inspired by the observation that on a smooth, compact Riemannian space with positive Ricci curvature, the distance between two small spheres of radius ϵ is smaller than the distance between their two centres (see [8] and references therein). The construction is entirely geometric and can be implemented in a straightforward way on simplicial manifolds, using geodesic link distance (or dual geodesic link distance) and the natural volume measure, counting the D-simplices. An important criterion that guided our search for a curvature observable is ease of implementation and low computational cost, in view of the fact that we are interested in evaluating it on non-infinitesimal neighbourhoods and in a quantum-gravitational context. Note that since it is natural to measure lengths and volumes in DT in terms of discrete units, measuring them is often reduced to counting, further simplifying implementation.

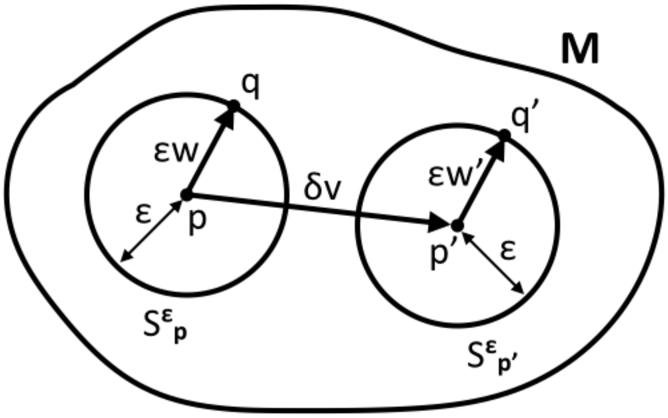

Figure 1: Two nearby spheres S^ϵ_p and $S^\epsilon_{p'}$ of radius ϵ whose centres are a small distance δ along the unit vector v apart. Parallel transport of a unit vector w at p along the geodesic of length δ connecting p and p' yields another unit vector w'. The distance between the points q and q' in flat space is equal to δ, while in the presence of curvature the lowest-order deviation from δ is given by formula (1).

3 A measure of curvature

To motivate our construction, we begin with the case of a smooth, D-dimensional Riemannian manifold $(M, g_{\mu\nu})$. The eventual application we have in mind is DT or CDT quantum gravity (the latter after "Wick rotation", such that the spacetimes summed over in the path integral have positive definite metric [1]). However, we do not see any obstacles to implementing it in other discrete metric settings. Consider two points p, $p' \in M$, which are a geodesic distance $\delta \geq 0$ apart. The two ϵ-spheres S^ϵ_p and $S^\epsilon_{p'}$ around p and p' consist of those points in M that are a distance $\epsilon \geq 0$ away from the centres p and p' respectively. The parameters δ and ϵ must be sufficiently small for the ϵ-spheres to have the topology of S^{D-1}-spheres and such that p' can be written uniquely as $p' = \exp_p(\delta v)$ in terms of the exponential map, where v is a unit vector in the tangent space T_pM.

There are various ways of defining the distance between the two spheres S^ϵ_p and $S^\epsilon_{p'}$. For example, parallel transport of tangent vectors in T_pM to $T_{p'}M$ along the geodesic connecting the centres p and p' can be used to identify points on the two spheres pairwise in a unique way. Suppose q is the image $q = \exp_p(\epsilon w)$ of the point p under the exponential mapping in the direction of the unit vector $w \in T_pM$. Parallel-transporting the vector w to p' yields another unit vector, $w' \in T_{p'}M$, which therefore points to a point q' on the sphere $S^\epsilon_{p'}$ in the sense that $q' = \exp_{p'}(\epsilon w')$ (see Fig. 1). Again, for this construction to be well-defined and unique, both δ and ϵ must be sufficiently small, which we will assume is the case. Assuming for simplicity that v and w are orthogonal, the distance between the two points q and q' is given by [7]

$$d(q, q') = \delta\left(1 - \frac{\epsilon^2}{2} K(v, w) + O(\epsilon^3 + \delta\epsilon^2)\right), \tag{1}$$

in the limit $(\delta, \epsilon) \to (0, 0)$, where the sectional curvature $K(v, w)$ is the Gaussian curvature of the two-dimensional surface of geodesics whose tangent vector at p lies in the span of v and w. Recall that the sectional curvature is defined in terms of the Riemann curvature tensor R and the scalar product $\langle \cdot, \cdot \rangle$ on M as

$$K(v, w) = \frac{\langle R(v, w)w, v\rangle}{\langle v, v\rangle\langle w, w\rangle - \langle v, w\rangle^2}, \tag{2}$$

where the denominator simplifies to 1 for orthonormal vectors v and w.

If S_p^ϵ is mapped to $S_{p'}^\epsilon$ using parallel transport, as described above, a point $q \in S_p^\epsilon$ and its image $q' \in S_{p'}^\epsilon$ are on average a distance

$$d(S_p^\epsilon, S_{p'}^\epsilon) = \delta\left(1 - \frac{\epsilon^2}{2D}\, Ric(v, v) + O(\epsilon^3 + \delta\epsilon^2)\right), \tag{3}$$

apart in the limit $(\delta, \epsilon) \to (0, 0)$ [8]. On the right-hand side of (3), $Ric(v, v)$ denotes the Ricci curvature associated with the unit vector v, given as the sum of the sectional curvatures of all planes containing v. In terms of an orthonormal basis $\{e_i,\, i = 1, \ldots, D\}$, it can be written as

$$Ric(e_1, e_1) = \sum_{i=2}^{D} K(e_1, e_i), \tag{4}$$

say. Expression (3) is obtained by integrating the point distances corresponding to all unit vectors w and dividing by the volume of the unit $(D-1)$-sphere. Equivalently, one can integrate over the sphere of radius ϵ with respect to the induced measure and divide by the sphere volume.

For a variety of reasons the prescription (3) is not particularly suited to extracting curvature from a simplicial manifold. Although the underlying parallel transport can be implemented straightforwardly, as was shown in [14] for the case of dynamical triangulations, local coordinate systems generally cannot be extended beyond pairs of adjacent building blocks. Geodesics between vertices further than one unit distance apart are in general non-unique. Moreover, if we consider only the distances between the *vertices* contained in nearby ϵ-spheres – as is natural in a simplicial context – their number will typically be different for different spheres.[3] This means that we cannot associate them pairwise in a one-to-one fashion, as was done to obtain (3).

Instead of the sphere distance (3) on smooth manifolds, we will use a more robust notion of "average sphere distance" that can be implemented also on more general metric spaces and not just in the limit of small distances. For this purpose, we will from now on interpret an "ϵ-sphere" S_p^ϵ as the set of all points at distance ϵ from a given centre point p, regardless of whether they form a sphere topologically. On a D-dimensional Riemannian manifold, the average sphere distance $\bar{d}$ of two ϵ-spheres centred at points p and p' is simply defined as

$$\bar{d}(S_p^\epsilon, S_{p'}^\epsilon) := \frac{1}{vol(S_p^\epsilon)} \frac{1}{vol(S_{p'}^\epsilon)} \int_{S_p^\epsilon} d^{D-1}q \, \sqrt{h} \int_{S_{p'}^\epsilon} d^{D-1}q' \, \sqrt{h'} \; d(q,q'), \tag{5}$$

where h and h' are the determinants of the metrics induced on the two $(D-1)$-dimensional "spheres", which are also used to compute the sphere volumes $vol(S)$, and $d(q,q')$ denotes the geodesic distance between the points q and q'. Note that $\bar{d}$ is not a proper distance in the mathematical sense. Although it is positive, symmetric and satisfies the triangle inequality, the average distance of an ϵ-sphere to itself does not vanish, unless $\epsilon = 0$.

For the definition (5) to be meaningful, it is not essential that the two spheres have the same radius, but this is the only case we will consider in the following. More specifically, our definition of "quantum Ricci curvature" will be based on pairs of overlapping spheres whose common radius is equal to the distance between their centres, $\epsilon = \delta$. This is not a unique choice, but a natural and convenient one if one is interested in a scalable curvature observable associated with a single scale δ. Adapting the definition (5) to a piecewise flat manifold made from equilateral simplices (a typical DT configuration), we have

$$\bar{d}(S_p^\epsilon, S_{p'}^\epsilon) = \frac{1}{N_0(S_p^\epsilon)} \frac{1}{N_0(S_{p'}^\epsilon)} \sum_{q \in S_p^\epsilon} \sum_{q' \in S_{p'}^\epsilon} d(q,q'), \tag{6}$$

where $N_0(S_p^\epsilon)$ is the number of vertices at link distance ϵ from the central vertex p and $d(q,q')$ now denotes the geodesic link distance between the vertices q and q', i.e. the number of links in the shortest path along links from q to q'.

We will extract a notion of *quantum Ricci curvature*[4] $K_q(p,p')$, associated with a pair of points p and p' separated by a distance δ, by comparing the average

---

[3] We should put "spheres" in inverted commas here, since the vertices and other (sub-)simplices at integer link distance ϵ from a chosen vertex do not in general form a topological $(D-1)$-sphere, but a disconnected space.

[4] The explicit construction and implementations described in what follows are not primarily of a quantum nature. However, the motivation and intended main application of this work is nonperturbative quantum gravity, justifying the label "quantum" (see also Sec. 7 for further comments). A genuine quantum-gravitational application will be presented in [15].

distance of the two δ-spheres centred at p and p' with δ according to

$$\frac{\bar{d}(S_p^\delta, S_{p'}^\delta)}{\delta} = c_q(1 - K_q(p,p')), \quad \delta = d(p,p'), \tag{7}$$

where c_q is a positive constant, which depends on the metric space under consideration, and K_q captures any nontrivial dependence on δ. This construction is similar to Ollivier's "coarse Ricci curvature" [7], specialized to a pair of spheres, but using the average distance (5) or (6) instead of the L^1-transportation distance. The latter is a genuine distance, but expensive to compute, because it is defined through an optimization. Since computability is an important requirement for the application we have in mind, we are using the average distance instead. In the next section, we will evaluate $\bar{d}/\delta$ for some classical, constantly curved model spaces and for non-infinitesimal distances and show that – unlike for the corresponding quantity in [7] – the constant c_q in (7) in general is not equal to 1.

4 Smooth model spaces

To develop a better understanding for the generalized Ricci curvature K_q, we will begin by evaluating it on smooth, constantly curved Riemannian manifolds, starting with the flat, spherical and hyperbolic spaces in $D = 2$ dimensions.

Consider a pair of spheres (circles) of radius ϵ in two-dimensional flat, Euclidean space, whose centres are a distance δ apart, not necessarily equal to ϵ. We will use an angular parameter $\alpha \in [0, 2\pi[$ to uniquely label points q_α along the sphere S_p^ϵ and the corresponding points q'_α on $S_{p'}^\epsilon$. Our convention is to measure the angle around p in anticlockwise direction from the geodesic connecting p and p'. Otherwise the situation is like that depicted in Fig. 1. For the sphere distance we compute

$$d(S_p^\epsilon, S_{p'}^\epsilon) = \frac{1}{2\pi}\int_0^{2\pi} d\alpha\, d(q_\alpha, q'_\alpha) = \frac{1}{2\pi}\int_0^{2\pi} d\alpha\, \delta = \delta, \tag{8}$$

independent of ϵ, since in flat space all point pairs (q_α, q'_α) are exactly a distance δ apart. The result (8) is consistent with the right-hand side of eq. (3), because in flat space $Ric(v,v)$ vanishes identically for all vectors v. The computation of the average distance of the two spheres involves a double integral,

$$\begin{aligned}\bar{d}(S_p^\epsilon, S_{p'}^\epsilon) &= \frac{1}{(2\pi)^2}\int_0^{2\pi} d\alpha \int_0^{2\pi} d\beta\, d(q_\alpha, q'_\beta)\\ &= \frac{1}{(2\pi)^2}\int_0^{2\pi} d\alpha \int_0^{2\pi} d\beta \sqrt{(\delta + \epsilon(\cos\beta - \cos\alpha))^2 + \epsilon^2(\sin\beta - \sin\alpha)^2},\end{aligned} \tag{9}$$

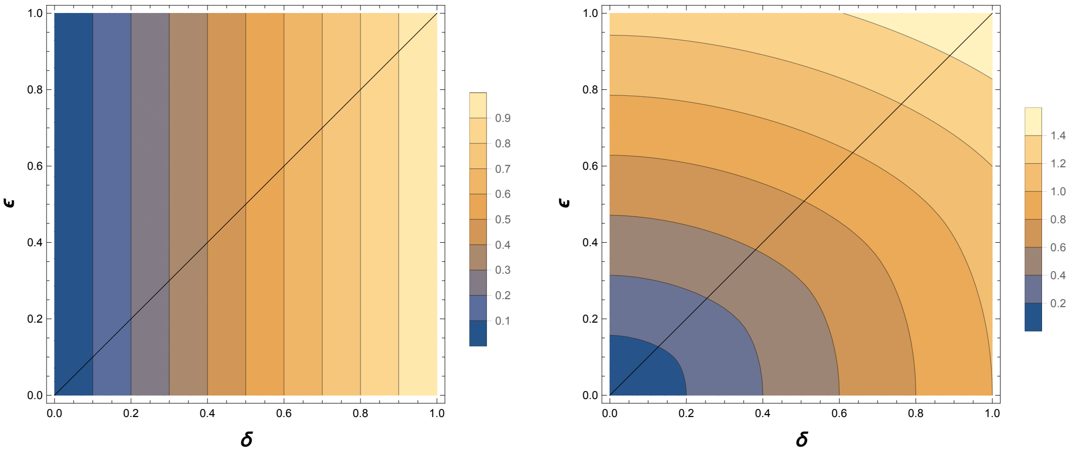

Figure 2: Contour plots of the distance between two circles on a two-dimensional flat space, as function of the circle radius ϵ and the distance δ of their centres. Left: sphere distance (8). Right: average sphere distance (9).

where the two angles α and β label arbitrary pairs of points $(q_\alpha, q'_\beta) \in S^\epsilon_p \times S^\epsilon_{p'}$. Since we are unable to evaluate the integrals in (9) analytically, we resort to a numerical evaluation. Fig. 2 shows contour plots of the sphere distance and the average sphere distance as functions of δ and ϵ. Note that for $\delta = \epsilon$, the case we will be considering for the quantum Ricci curvature, expression (9) is purely linear in δ. This corresponds to the diagonal in the plot on the right in Fig. 2. Numerically, the average sphere distance in this case evaluates to

$$\bar{d}(S^\delta_p, S^\delta_{p'}) \approx 1.5746\,\delta \quad \text{(flat case)}. \tag{10}$$

Comparing with the sphere distance of relation (8), we see that the constant prefactor of δ has changed from 1 to $c_q \approx 1.5746$. For smooth Riemannian manifolds, the coefficient of δ in the power expansion of $\bar{d}(S^\delta_p, S^\delta_{p'})$ is universal and depends only on the dimension of M. For instance, an analogous calculation for the average sphere distance (for $\epsilon = \delta$) in three-dimensional flat space yields $\bar{d} \approx 1.6250\,\delta$.

Next, we consider pairs of ϵ-circles on a constantly curved two-sphere of embedding radius ρ. In other words, we can think of the two-sphere as consisting of all points $(x, y, z) \in \mathbb{R}^3$ satisfying $x^2 + y^2 + z^2 = \rho^2$. Points on the two-sphere can also be described by two angles $\theta \in [0, \pi]$ and $\varphi \in [0, 2\pi[$. Recall that geodesics on S^2 are arcs of great circles and that the geodesic distance between two points (θ_i, φ_i), $i = 1, 2$, is given by

$$d((\theta_1, \varphi_1), (\theta_2, \varphi_2)) = \rho \arccos(\cos\theta_1 \cos\theta_2 + \sin\theta_1 \sin\theta_2 \cos(\varphi_2 - \varphi_1)). \tag{11}$$

The sphere distance of two ϵ-circles whose centres are a distance δ apart is given

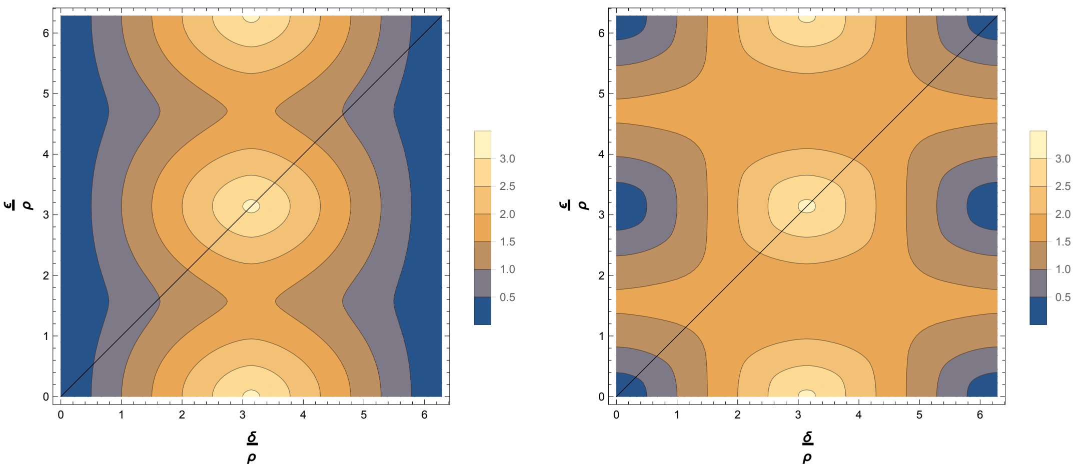

Figure 3: Contour plots of the distance between two circles on a two-dimensional space of constant positive curvature, as function of the circle radius ϵ and the distance δ of their centres, both rescaled by the curvature radius ρ. Left: sphere distance (12). Right: average sphere distance (14).

by

$$d(S^\epsilon_p, S^\epsilon_{p'}) = \frac{1}{2\pi}\int_0^{2\pi} d\alpha\; \rho\, \arccos\Big(\cos\tfrac{\delta}{\rho} + \sin^2\alpha\, \sin^2(\tfrac{\epsilon}{\rho})\,(1-\cos\tfrac{\delta}{\rho})\Big). \tag{12}$$

Expanding the integrand on the right-hand side of (12), which is the curved-space analogue of the distance $d(q_\alpha, q'_\alpha)$ in the flat-space integral (8), for small δ and ϵ leads to

$$\begin{aligned}\frac{\delta}{2\pi}\int_0^{2\pi} d\alpha \Big(1 - \tfrac12\big(\tfrac{\epsilon}{\rho}\big)^2\sin^2\alpha + \big(\tfrac{\epsilon}{\rho}\big)^4\big(\tfrac16\sin^2\alpha - \tfrac18\sin^4\alpha\big) - \tfrac1{24}\big(\tfrac{\epsilon}{\rho}\big)^2\big(\tfrac{\delta}{\rho}\big)^2\sin^2\alpha + \text{h.o.}\Big)\\ = \delta\Big(1-\tfrac14\big(\tfrac{\epsilon}{\rho}\big)^2 + \tfrac{7}{192}\big(\tfrac{\epsilon}{\rho}\big)^4 - \tfrac{1}{48}\big(\tfrac{\epsilon}{\rho}\big)^2\big(\tfrac{\delta}{\rho}\big)^2 + \text{h.o.}\Big),\end{aligned} \tag{13}$$

where h.o. denotes terms of combined δ- and ϵ-order of at least six. Given that the Ricci curvature $Ric(v,v)$ on the two-sphere is $1/\rho^2$ for any unit vector v, we see that the integration result in (13) is consistent with the general formula (3) for $D=2$. Considering next the average sphere distance and again using eq. (11), we find

$$\begin{aligned}\bar{d}(S^\epsilon_p, S^\epsilon_{p'}) = \frac{\rho}{(2\pi)^2}\int_0^{2\pi} d\alpha \int_0^{2\pi} d\beta\; \arccos\Big(\sqrt{1-\sin^2(\tfrac{\epsilon}{\rho})\sin^2\alpha}\sqrt{1-\sin^2(\tfrac{\epsilon}{\rho})\sin^2\beta}\\ \times\cos\big(\tfrac{\delta}{\rho} + \arctan\big(\tan\tfrac{\epsilon}{\rho}\cos\beta\big) - \arctan\big(\tan\tfrac{\epsilon}{\rho}\cos\alpha\big)\big) + \sin^2(\tfrac{\epsilon}{\rho})\sin\alpha\,\sin\beta\Big).\end{aligned} \tag{14}$$

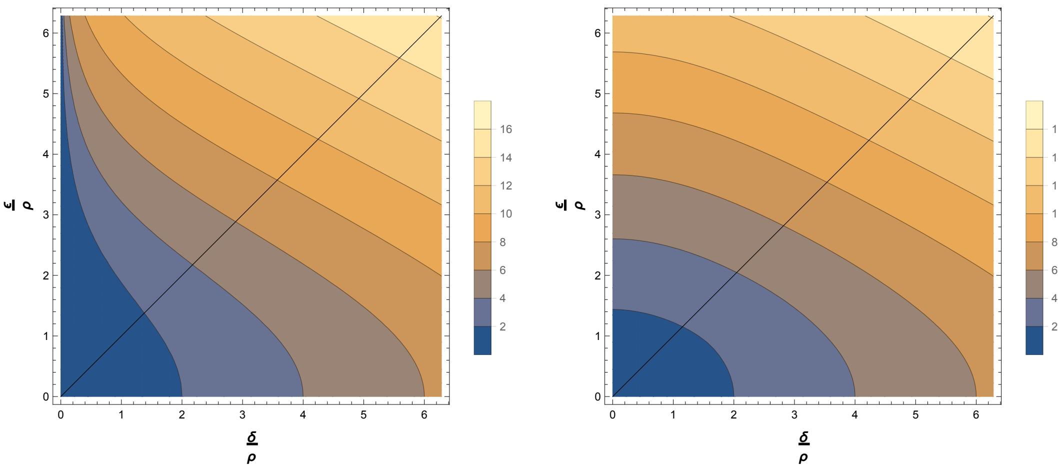

Figure 4: Contour plots of the distance between two circles on a two-dimensional space of constant negative curvature, as function of the circle radius ϵ and the distance δ of their centres, both rescaled by the curvature radius ρ. Left: sphere distance (17). Right: average sphere distance (19).

Setting $\epsilon = \delta$ and expanding this expression for small δ results in

$$\bar{d}(S_p^\delta, S_{p'}^\delta) \approx \delta\Big(1.5746 - 0.1440\big(\tfrac{\delta}{\rho}\big)^2 - 0.0239\big(\tfrac{\delta}{\rho}\big)^4 + O\Big(\big(\tfrac{\delta}{\rho}\big)^6\Big)\Big), \tag{15}$$

where the coefficients were determined by numerical integration. At linear order in δ the same constant appears as in the flat case of eq. (10). The next-to-leading order is proportional to the Ricci curvature with a negative coefficient, which is qualitatively similar to the behaviour (13) of the corresponding expansion of the sphere distance. The contour plots for both types of sphere distance are shown in Fig. 3, as functions of δ/ρ and ϵ/ρ, both taking values in the interval $[0, 2\pi]$. Note that the plots are symmetric under both $\delta \mapsto 2\pi\rho - \delta$ and $\epsilon \mapsto 2\pi\rho - \epsilon$, a property that can be read off easily from their analytic expressions (12) and (14).

Lastly, we consider circle distances on the negatively curved hyperbolic space in two dimensions, defined as the set of all points $(x, y, z) \in \mathbb{R}^3$ satisfying $-x^2 - y^2 + z^2 = \rho^2$ and $z > 0$. Points on this space can be parametrized by a hyperbolic angle $\theta \in [0, \infty[$ and an ordinary angle $\varphi \in [0, 2\pi[$, which are related to the Euclidean coordinates by $\theta = \mathrm{arccosh}(z/\rho)$ and $\varphi = \arctan(y/x)$. The geodesic distance between two such points (θ_i, φ_i), $i = 1, 2$, is given by

$$d((\theta_1, \varphi_1), (\theta_2, \varphi_2)) = \rho\, \mathrm{arccosh}(\cosh\theta_1 \cosh\theta_2 - \sinh\theta_1 \sinh\theta_2 \cos(\varphi_2 - \varphi_1)). \tag{16}$$

From this, we obtain the sphere distance of two ϵ-circles at distance δ as a straightforward hyperbolic version of formula (12), namely,

$$d(S_p^\epsilon, S_{p'}^\epsilon) = \frac{1}{2\pi} \int_0^{2\pi} d\alpha\; \rho\, \mathrm{arccosh}(\cosh\tfrac{\delta}{\rho} + \sin^2\!\alpha\, \sinh^2(\tfrac{\epsilon}{\rho})\, (\cosh\tfrac{\delta}{\rho} - 1)), \tag{17}$$

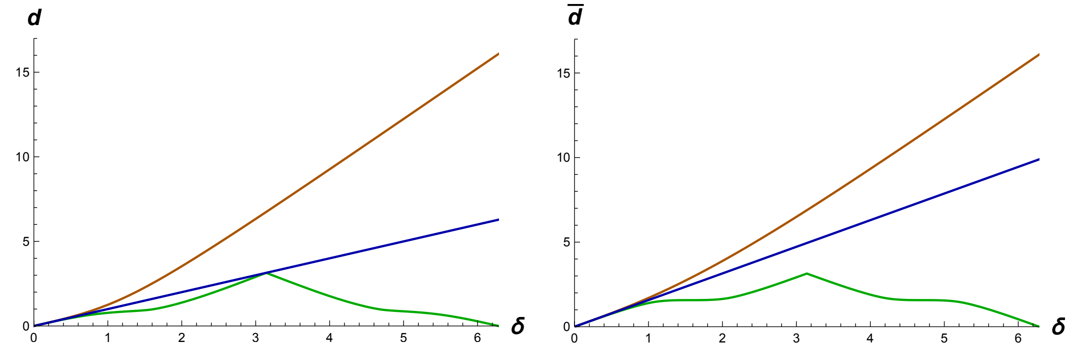

Figure 5: Comparing sphere distance (left) and average sphere distance (right) for $\epsilon = \delta$, as function of $\delta \in [0, 2\pi]$, for the three constantly curved model spaces: hyperbolic (top), flat (middle) and spherical (bottom). The curvature radius ρ has been set to 1.

whose expansion for small δ and ϵ is given by

$$\frac{\delta}{2\pi}\int_0^{2\pi} d\alpha \left(1+\tfrac{1}{2}\big(\tfrac{\epsilon}{\rho}\big)^2 \sin^2\!\alpha + \big(\tfrac{\epsilon}{\rho}\big)^4 \left(\tfrac{1}{6}\,\sin^2\!\alpha - \tfrac{1}{8}\,\sin^4\!\alpha\right) - \tfrac{1}{24}\big(\tfrac{\epsilon}{\rho}\big)^2 \big(\tfrac{\delta}{\rho}\big)^2 \sin^2\!\alpha + \text{h.o.}\right)$$
$$= \delta\left(1+\tfrac{1}{4}\big(\tfrac{\epsilon}{\rho}\big)^2 + \tfrac{7}{192}\big(\tfrac{\epsilon}{\rho}\big)^4 - \tfrac{1}{48}\big(\tfrac{\epsilon}{\rho}\big)^2\big(\tfrac{\delta}{\rho}\big)^2 + \text{h.o.}\right), \tag{18}$$

which to this order is identical with the corresponding formula (13), apart from the sign of the term proportional to $\delta\epsilon^2$. Comparing this term with eq. (3) leads to $Ric(v,v) = -1/\rho^2$, which is the well-known result for the Ricci curvature on hyperbolic space. The average sphere distance in hyperbolic space is given by the double integral

$$\bar{d}(S_p^\epsilon, S_{p'}^\epsilon) = \frac{\rho}{(2\pi)^2}\int_0^{2\pi} d\alpha \int_0^{2\pi} d\beta\, \operatorname{arccosh}\Big((\cos\beta - \cos\alpha)\sinh\tfrac{\epsilon}{\rho}\cosh\tfrac{\epsilon}{\rho}\sinh\tfrac{\delta}{\rho}$$
$$+\cosh^2\!\big(\tfrac{\epsilon}{\rho}\big)\cosh\tfrac{\delta}{\rho} - \sinh^2\!\big(\tfrac{\epsilon}{\rho}\big)\Big(\sin\alpha\,\sin\beta + \cos\alpha\,\cos\beta\,\cosh\tfrac{\delta}{\rho}\Big)\Big). \tag{19}$$

Setting $\epsilon = \delta$ and expanding this expression for small δ gives

$$\bar{d}(S_p^\delta, S_{p'}^\delta) \approx \delta\Big(1.5746 + 0.1440\big(\tfrac{\delta}{\rho}\big)^2 - 0.0239\big(\tfrac{\delta}{\rho}\big)^4 + O\Big(\big(\tfrac{\delta}{\rho}\big)^6\Big)\Big), \tag{20}$$

where the coefficients were again determined by numerical integration. Comparing this with the corresponding expansion (15) for the spherical case, we observe the same behaviour as for the sphere distances: the expansions to this order are the same, only the term proportional to δ^3 has its sign reversed because of the opposite sign of the Ricci curvature.

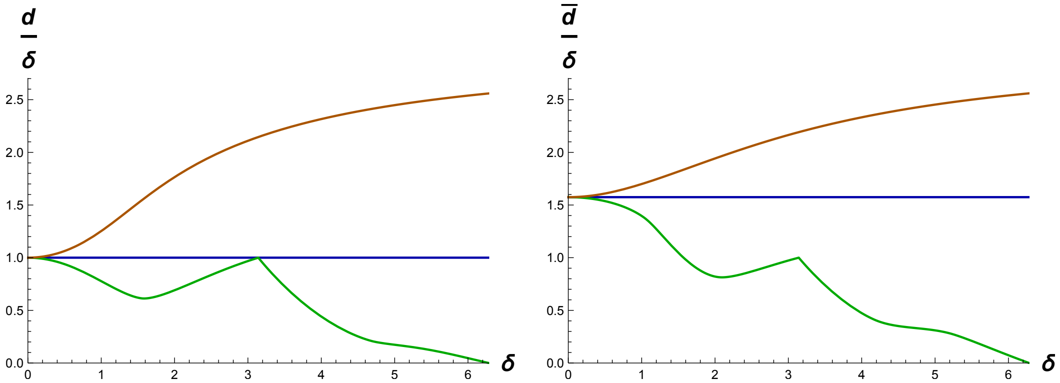

Figure 6: Comparing the normalized versions of sphere distance (left) and average sphere distance (right) for $\epsilon = \delta$, as function of $\delta \in [0, 2\pi]$, for the three constantly curved model spaces: hyperbolic (top), flat (middle) and spherical (bottom). The curvature radius ρ has been set to 1.

Fig. 4 juxtaposes the behaviour of the sphere distance and the average sphere distance as functions of both δ/ρ and ϵ/ρ. The ranges of these hyperbolic angles have been chosen identical to the sphere case of Fig. 3 for ease of comparison. The three plot pairs of Figs. 2, 3 and 4 illustrate the behaviour of the two sphere distances $d(S_p^\epsilon, S_{p'}^\epsilon)$ and $\bar{d}(S_p^\epsilon, S_{p'}^\epsilon)$ for large values of δ and ϵ, and specifically the qualitative similarity along the diagonal $\delta = \epsilon$ in all three cases, which is relevant for our definition of quantum Ricci curvature. Fig. 5 shows the behaviour along the diagonal of the sphere distance and the average sphere distance for all three two-dimensional model spaces, while Fig. 6 compares the corresponding normalized distances, where we have divided by δ. Again, the graphs illustrate the similarities in behaviour of the sphere and the average sphere distances. One feature of the latter is that the three curves are genuinely disjoint for $\delta > 0$. For the homogeneous and isotropic spaces we are considering presently, we can simplify the scaling relation (7) to

$$\frac{\bar{d}(S_p^\delta, S_{p'}^\delta)}{\delta} = c_q(1 - K_q(\delta)), \tag{21}$$

We observe here that the constant c_q can be determined uniquely and assumes the same value $c_q \approx 1.5746$ for all of the three smooth model spaces in two dimensions. Furthermore, we have established that the "quantum Ricci curvature" $K_q(\delta)$ vanishes on flat space, and has a nontrivial behaviour on the spaces of constant positive and negative curvature (Fig. 6). It is negative and monotonically decreasing on the negatively curved space, and is positive and monotonically increasing up to $\delta/\rho \approx 2.095$ on the positively curved space.

The two curves pertaining to the hyperbolic case in Fig. 6 both asymptote to

3, as can also be established straightforwardly by considering the limit $\delta \to \infty$ of the expressions for d/δ and $\bar{d}/\delta$ in eqs. (17) and (19). The plots on the right in both Figs. 5 and 6 will serve as reference when we determine the curvature properties of more general spaces.

5 Curvature on regular lattices

In this and the next section we will develop a better understanding of the behaviour of the quantum Ricci curvature on continuous but non-smooth metric spaces. Since the eventual application we have in mind are Causal Dynamical Triangulations, we will focus on piecewise flat spaces consisting of a single type of equilateral building block. In such a setting, the evaluation of the curvature assumes a combinatorial character, because volume measurements reduce to a counting of building blocks (which all have equal size), and measuring the geodesic (link) distance between two vertices v_1 and v_2 by definition amounts to a counting of one-dimensional edges in the shortest path linking v_1 and v_2. We treat these spaces as approximations to smooth spaces and therefore will be particularly interested in the behaviour of curvature on scales that are large compared to the length a of an edge of a building block. An important part of our analysis will be to obtain an estimate of the scale δ above which short-scale, so-called "lattice artefacts" become irrelevant, by which one means a dependence of the results on the specifics of the shape of the individual building blocks and of the local "gluing rules" by which the metric spaces are assembled from them.

The spaces we investigate in this section are flat, regular lattices, and can be regarded as tilings or subdivisions into equal building blocks of flat, Euclidean space. We will treat the square, hexagonal and honeycomb lattices in two dimensions and the cubic and face-centred cubic lattices in three dimensions. To determine their quantum Ricci curvature, we will use a straightforward implementation of the average sphere distance (5) on these spaces, which is given by formula (6) for two overlapping spheres S^δ whose radii are equal to the distance between their centres, $\epsilon = \delta$. Some of the calculations are sufficiently simple to be done analytically, as we will see below.

To illustrate what is involved computationally, we will first consider the two-dimensional square lattice. Its vertices are all points with integer coordinates (x, y), and the geodesic link distance between two such points is the number of edges of the shortest path between them. Fig. 7 shows a pair of overlapping δ-spheres, whose average distance one wants to compute as a function of the scale δ. Since the set-up is invariant under discrete lattice translation in both the x- and y-directions, one can without loss of generality put the centre of the sphere S_p^δ at the origin, such that $p = (0, 0)$. Note that the link distance between two

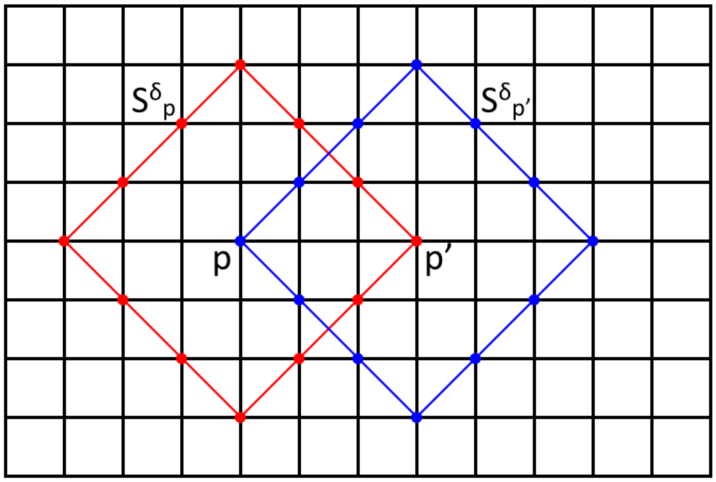

Figure 7: Two overlapping spheres S^δ_p and $S^\delta_{p'}$ of radius $\delta\!=\!3$ on a square lattice, whose centre vertices p and p' are a link distance $\delta\!=\!3$ apart. Each sphere consists of 12 vertices. The diagonal edges between the sphere vertices are drawn for ease of visualization only and are not part of the spheres or the underlying lattice.

points $p = (x, y)$ and $p' = (x', y')$ is given by

$$d(p, p') = |x - x'| + |y - y'|. \tag{22}$$

As an intermediate step to computing the sphere distance, one can work out the distance of an arbitrary point (x, y) to the δ-sphere S^δ_0 centred at $(0, 0)$, defined as $d(S^\delta_0, p) := \sum_{q \in S^\delta_0} d(q, p)$. Because of the lattice symmetries, it is sufficient to compute this distance for a point $p = (x, y)$ lying in the positive quadrant, where $x \geq 0$ and $y \geq 0$. Distinguishing between four different cases, depending on the location of p, one finds

$$d(S^\delta_0, p) = \begin{cases} 4\delta(x+y), & x \geq \delta,\, y \geq \delta \\ 4\delta x + 2\delta^2 + 2y^2, & x \geq \delta,\, 0 \leq y < \delta \\ 4\delta y + 2\delta^2 + 2x^2, & 0 \leq x < \delta,\, y \geq \delta \\ 4\delta^2 + 2x^2 + 2y^2, & 0 \leq x < \delta,\, 0 \leq y < \delta. \end{cases} \tag{23}$$

If the centres of the two spheres share the same x- or the same y-coordinate, the shortest path between their centres is a straight line segment, as in the example shown in Fig. 7. Taking into account that the volume of a δ-sphere is given by 4δ (the number of vertices contained in the sphere of radius δ), one obtains for the average sphere distance in this particular case

$$\bar{d}(S^\delta_p, S^\delta_{p'}) = \frac{7}{4}\,\delta + \frac{1}{8\,\delta} = 1.75\,\delta + 0.125\,\frac{1}{\delta}. \tag{24}$$

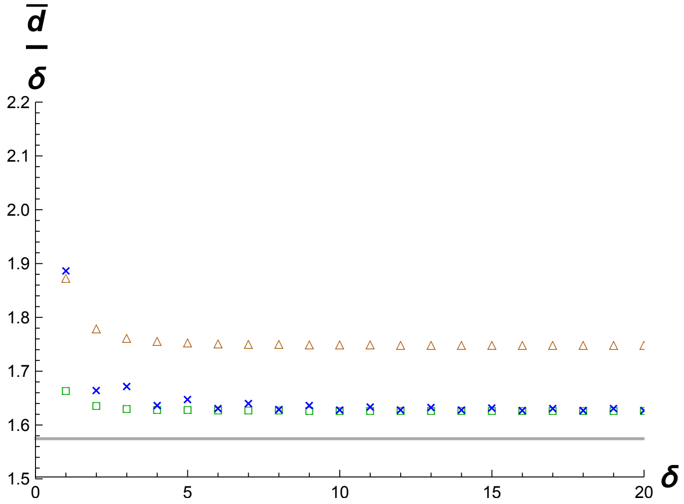

Figure 8: Normalized average sphere distance $\bar{d}(S_p^\delta, S_{p'}^\delta)/\delta$ on the square, hexagonal and honeycomb lattices in two dimensions, marked by triangles, squares and crosses respectively, as function of δ. The straight horizontal line is that of flat continuum space, and is included for comparison.

Recall that in the continuum case of the previous section, the corresponding expression for the flat case had a term linear in δ, and no higher-order terms. Eq. (24) for the square lattice has the same features, but with an additional term proportional to $1/\delta$. It will be suppressed with increasing δ and therefore can be interpreted as a short-scale lattice discretization effect. On the hexagonal lattice, which consists of equilateral triangles, the analogous scaling relation turns out to be

$$\bar{d}(S_p^\delta, S_{p'}^\delta) = \frac{44}{27}\,\delta + \frac{1}{27\,\delta} \approx 1.6296\,\delta + 0.0370\,\frac{1}{\delta}, \tag{25}$$

where again we have considered overlapping spheres whose centres are connected by a straight sequence of edges. The fact that the coefficients of the linear terms in (24) and (25) differ from the continuum value of 1.5746 is due to two effects. First, the use of link distance instead of Euclidean distance leads to an overestimation of distances except those along straight sequences of links. Second, the shape of a "sphere" on a square or hexagonal lattice differs significantly from that of a round sphere, which affects results. The fact that a hexagon is closer in shape to a sphere may explain that the coefficient is closer to the continuum value.

We have also investigated the honeycomb lattice. By eliminating every other vertex from it – keeping only vertices whose pairwise link distance is even – one obtains a hexagonal lattice. This implies that the results for the average sphere distance on the honeycomb lattice for even δ will be the same as two times those for the hexagonal lattice for $\delta/2$. The case of odd δ is slightly more involved and

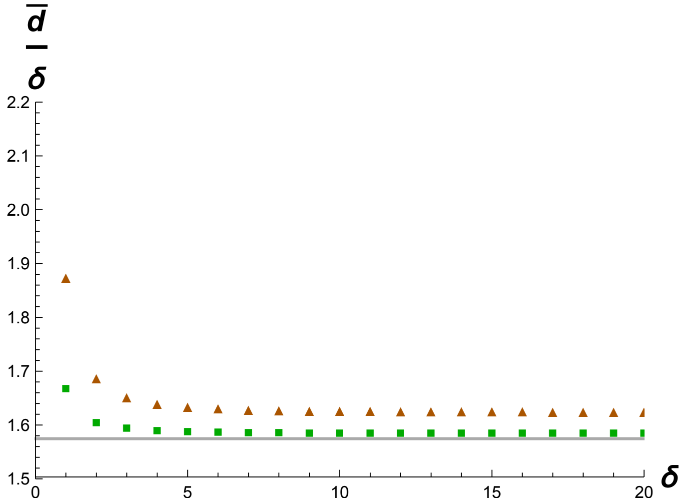

Figure 9: Normalized average sphere distance $\bar{d}(S_p^\delta, S_{p'}^\delta)/\delta$ on two-dimensional flat lattices, averaged over lattice directions as described in the text. Triangles and squares mark the data points for the square and hexagonal lattices respectively. The straight horizontal line is that of flat continuum space.

can be treated separately. The complete result for the honeycomb lattice is given by

$$\bar{d}(S_p^\delta, S_{p'}^\delta) = \begin{cases} \frac{44}{27}\,\delta + \frac{1}{18} + \frac{7}{27\,\delta} - \frac{1}{18\,\delta^2} & \delta \text{ odd}, \\ \frac{44}{27}\,\delta + \frac{4}{27\,\delta} & \delta \text{ even}. \end{cases} \tag{26}$$

Fig. 8 shows the plots for the normalized average sphere distance $\bar{d}/\delta$ for the three flat lattices. We observe that in all cases the curves start out at slightly elevated values for small δ and then quickly settle down to a constant, as one would expect from a flat-space behaviour, where the value of the constant depends on the lattice chosen. These differences are to be expected, because on large scales the geodesic link distance scales with a different constant relative to the "true" geodesic distance in the continuum, depending on the type of lattice. If one wanted to take the short-scale geometry of these lattices seriously, one would say that they exhibit negative quantum Ricci curvature for small δ. Note that this phenomenon also occurs for the coarse Ollivier-Ricci curvature, which is negative when evaluated at $\delta = 1$ on a regular honeycomb lattice, say [16].

As mentioned above, our computations for the average sphere distance did not use the most general configuration of two overlapping spheres at distance δ, but only pairs of spheres whose centres are aligned along a straight line. In the earlier example of the square lattice depicted in Fig. 7, these would be pairs of spheres whose centres share the same x-coordinate, $p = (0, 0)$ and $p' = (0, \delta)$, or the same y-coordinate, with $p = (0, 0)$ and $p' = (\delta, 0)$. For the square and hexagonal lattices, we have repeated the calculation of $\bar{d}$ for the most general case, where the shortest path connecting the two centres can be a zigzag path.[5] On the square lattice, this would be the case for centre coordinates $p = (0,0)$ and $p' = (x,y)$ with $0 < x < \delta$, $0 < y < \delta$ and $x + y = \delta$, say. For a given distance δ, there are now many more sphere configurations to consider and an analytic evaluation is less straightforward. Instead, we have used the computer to calculate $\bar{d}/\delta$ based on this more general set of configurations. One would a priori expect that the underlying improved averaging over lattice directions leads to results closer to those of the continuum. This is indeed the case, as illustrated by the data shown in Fig. 9. The convergence behaviour is similar to that depicted in Fig. 8, but the constant asymptotic values 1.625 for the square lattice and 1.583 for the hexagonal lattice are closer to the value found in the continuum.

Turning finally to three-dimensional lattices, a similar derivation for the flat cubic lattice leads to an average sphere distance

$$\bar{d}(S_p^\delta, S_{p'}^\delta) = \frac{82\delta^5 + 90\delta^3 + 23\delta}{10(1+2\delta^2)^2} = \frac{41}{20}\,\delta + \frac{1}{5\,\delta} + \mathcal{O}((\tfrac{1}{\delta})^3), \tag{27}$$

where again we have considered only those configurations where the centres of the two overlapping two-spheres are separated by a straight sequence of δ lattice edges. To determine the distance between the spheres, we averaged over the distances between all pairs of vertices contained in the two spheres. The result (27) strongly resembles the behaviour in two dimensions, with an asymptotically linear behaviour in δ and positive "correction terms" for small δ. Again the coefficient of the linear term, $41/20 = 2.05$ is larger than the corresponding continuum value 1.6250.

We have also investigated the face-centred cubic lattice, which is associated with a closest packing of spheres in three dimensions. To construct it, one starts with a single layer of spheres, arranged in a closest packing with respect to two dimensions, the x-y-plane, say. The centres of the spheres can be thought of as the vertices of a two-dimensional lattice, whose edges correspond to pairs of neighbouring spheres. Since each sphere has six neighbours, this results in the two-dimensional regular hexagonal lattice we already discussed above. On top of the lowest layer, we stack another, identical layer of spheres in the z-direction. Since there are twice as many gaps in the lower layer as there are spheres in the second layer, there are two possibilities of placing the second layer, corresponding to two different displacements of the spheres relative to those of the first layer. Each sphere in the lower layer has three neighbouring spheres in the second

---

[5] On the honeycomb lattice, there are no straight paths in the sense of Euclidean flat space, but there is an analogue of the preferred "straight" directions of the other lattice types, which was used to compute the formulas (26).

layer, and vice versa. There are two different choices for how to add a third layer of spheres. The first possibility is to align the centres of the spheres in the x-y-directions with those of the first layer, and the second possibility – the one chosen by us – is to displace the centres in the same direction and by the same amount in the x-y-plane as in the step from the first to the second layer. Repeating the same step for subsequent layers, one obtains a regular three-dimensional lattice with discrete period 3 in the z-direction, the so-called face-centred cubic lattice, all of whose vertices have order 12.

We were able to derive an explicit formula for the average sphere distance on this lattice, for the case that the centres of the spheres lie in the same hexagonal layer and are connected by a straight sequence of lattice edges. The result is given by

$$\bar{d}(S_p^\delta, S_{p'}^\delta) = \frac{3547\delta^5 + 1705\delta^3 + 148\delta}{80(1+5\delta^2)^2} = \frac{3547}{2000}\,\delta + \frac{1431}{10000\,\delta} + \mathcal{O}((\tfrac{1}{\delta})^3), \tag{28}$$

and therefore structurally similar to the result for the cubic lattice, eq. (27). The coefficient of the linear term is $3547/2000 \approx 1.77$, which is closer to the continuum value than that of the cubic lattice. This resembles the situation we encountered in two dimensions, namely, that the lattice with the higher coordination number (in this case 12 instead of 8) appears to give a better approximation to the continuum.

To summarize, evaluating the average sphere distance on several flat regular lattices, viewed as discrete approximations to continuum flat space, leads to consistent results: up to short-distance lattice artefacts, which are confined to a region $\delta \lesssim 5$, the behaviour of $\bar{d}$ is essentially linear in δ, compatible with a vanishing quantum Ricci curvature $K_q(\delta)$ in eq. (21). In all the cases we have investigated, the constant c_q in the same scaling law is in the vicinity of and larger than the corresponding continuum value.

6 Curvature on random triangulations

As a next step we consider classes of random triangulations that in general carry nonvanishing quantum Ricci curvature. They are still well-behaved in the sense of not deviating too much from smooth spaces. The triangulations are two-dimensional, made of equilateral Euclidean triangles and are obtained from Delaunay triangulations of flat and constantly curved spaces of either signature. Their small-scale behaviour depends on the local random structure, but their properties on large scales reflect the geometry of the smooth spaces they are approximating.

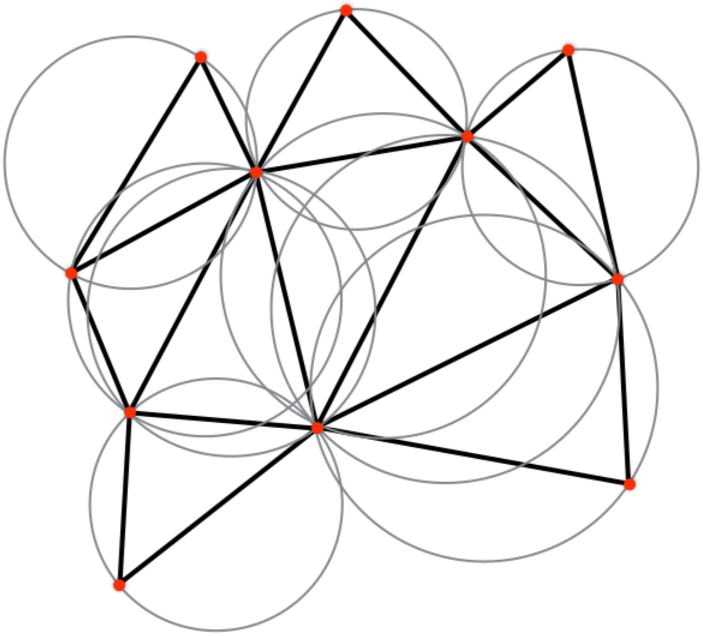

Figure 10: A Delaunay triangulation in the plane, together with the circumcircles of its constituting triangles. By definition, no circumcircle contains any vertices of the triangulation in its interior.

Recall that a Delaunay triangulation in the plane is a triangulation of a finite point set $P \subset \mathbb{R}^2$ (constituting the vertices of the triangulation) if the circumcircle of every triangle contains no points of P in its interior. The circumcircle of a triangle is defined as the unique circle containing the three vertices of the triangle (see Fig. 10). Because of their nice geometric properties Delaunay triangulations appear in numerous applications. Compared to other triangulations of the same point set $P \subset \mathbb{R}^2$, the (essentially unique[6]) Delaunay triangulation of P maximizes the minimum angle, which means that thin, elongated triangles tend to be avoided. Note that analogous constructions of Delaunay triangulations exist in higher dimensions too.

In all cases, we will proceed in three steps, first generating a point set P with the help of a Poisson disc sampling. Poisson disc sampling generates a tightly packed point collection with a specified minimal distance $d_{\min}$ between any two of its points. Second, we construct a Delaunay triangulation that has these points as vertices. Because of the nature of the Poisson disc sampling, the

---

[6] The uniqueness is up to sets of more than $D+1$ vertices (in D dimensions) that fall on the same circle, without other vertices inside the circle. For a local configuration of this type, any valid internal substructure will lead to a Delaunay triangulation. In our construction, this degeneracy cannot occur.

edge lengths of this Delaunay triangulation are clustered relatively compactly around some average edge length. The third step consists in setting all edge lengths to 1 and thereby making the triangulations equilateral before starting to measure average sphere distances on them. This is motivated by the fact that we are interested in exploiting the simplicity of the combinatorial aspects of the prescription (6), which also holds in CDT quantum gravity, the physical application we are primarily interested in. Adjusting the edge lengths in this way will alter the local metric properties of the triangulations. However, this appears to have only a mild effect, which is confined to smaller scales, as we will see when examining the results of the quantum Ricci curvature measurements.

6.1 Flat case

We begin by sketching the procedure for the case of random triangulations approximating flat space, where we will use an auxiliary regular grid to speed up the Poisson disc sampling, following [17]. We refer the interested reader to reference [17] for further details on the construction. For the process to be meaningful, we must confine ourselves to a finite region of flat space, which we choose to be a square of approximate side length 100 $d_{\min}$. All subsequent operations will take place inside this square.[7] Furthermore, the square is overlaid by a regular square grid whose cells have side length $d_{\min}/\sqrt{2}$. This ensures that each cell will contain at most one point of the point set P to be constructed. The grid forms an auxiliary structure in the Poisson disc sampling and the subsequent triangulation.

Starting from an initial point p_0 at the centre of the square, say, we systematically build up a point set P. The process is characterized by the minimal distance $d_{\min}$ and by another integer k, which is chosen a priori and will determine the density of P. A step in the algorithm consists in picking a point p from the set of points already selected to lie in P. Given p, we randomly pick a new point q in the annulus between radii $d_{\min}$ and $2\,d_{\min}$ around p. If the Euclidean distance of q to any other already selected point is smaller than or equal to $d_{\min}$, the point is discarded, otherwise it is added to the set of points selected to lie in P. For fixed p, we generate k new random points in this way, which we either keep or discard. A larger k will lead to a denser and more uniform set P at the end of the algorithm, but also to an increase in the overall time needed to generate the points. We used $k = 30$. Next, another point p' is taken from the already selected point set and the procedure is repeated by choosing k times a random point in

---

[7] Since we have only treated the computation of sphere distances for interior points, we make sure that during measurements we stay well away from any boundaries. It would take us too far to give a detailed description of the boundary construction for our triangulations. Suffice it to say that it involved a one-dimensional Poisson process with minimal distance $d_{\min}$, and that we performed detailed numerical tests to make sure unwanted boundary effects are negligible.

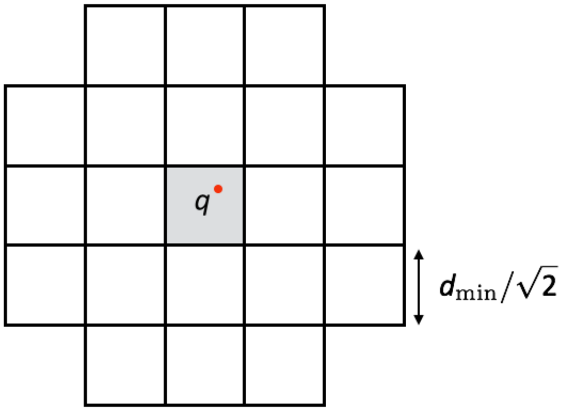

Figure 11: Using the auxiliary square lattice: during the construction of the initial point set P, only the 20 cells shown surrounding the cell of a new candidate point q need to be checked for the presence of other points within radius $d_{\min}$.

the annulus around p'. Note that a point p can only serve once as the base point for such a search, lying at the centre of an annulus. The process ends when all points in the selected set have acted as a base point. The final point set is the searched-for P. Note that the presence of the grid structure simplifies the test of whether a point q should be discarded, because only a finite number of cells (20 cells excluding the cell where q itself is located) around q need to be checked for points that are potentially too close to q, see Fig. 11 for illustration.

The same grid structure is also used during the construction of the Delaunay triangulation of a given set P. Following [17], we first generate a discrete clustering of all cells, where each cell C is associated with the vertex in P that is closest to the centre of C in terms of Euclidean distance. This results in a clustering of the cells of the square grid, with as many clusters as there are vertices in P. The algorithm proceeds by examining each vertex *of the square grid* in turn, by picking for each cell its lower left-hand corner point, say. Each corner point x is then assigned an index between 1 and 4, counting the number of distinct clusters meeting at x. The index is 1 if all four cells meeting at x belong to the same cluster, it is 2 if the four cells belong to two different clusters, and analogous for index 3 and 4, see [17] for further explanations and illustrations.

The point of this clustering is that it allows for the straightforward construction of a triangulation that is “almost Delaunay”. To obtain it, we draw for each corner point with index 3 a triangle connecting the corresponding three vertices of P. Next, we draw for each corner point with index 4 the quadrilateral spanned by the corresponding four vertices. There are then two ways to add an interior link to obtain a pair of adjacent triangles. Of those, we choose the interior link for which the angle sum of the quadrilateral at the corners met by the link is larger than π. This is a necessary condition for a Delaunay triangulation, and equivalent to the circumcircle condition mentioned earlier. After dealing with all corner points of index 3 and 4 in this manner, one obtains a triangulation which in general is not quite a Delaunay triangulation, but can be transformed into one by systematically checking the local Delaunay property for every link, and performing link flips wherever necessary, as shown in reference [17].

6.2 Non-flat case

The procedure outlined in the previous subsection must be adapted for random triangulations approximating non-flat spaces. The first step will again be to construct a point set P by Poisson disc sampling, this time on a constantly curved, smooth model space, the two-dimensional sphere or (a subset of) two-dimensional hyperbolic space. In both cases we have found it convenient to parametrize points in these spaces by the Cartesian coordinates (x, y, z) of their embeddings into $\mathbb{R}^3$, as described in Sec. 4 above. Introducing the notation

$$q_1 \cdot q_2 \equiv (x_1, y_1, z_1) \cdot (x_2, y_2, z_2) = x_1 x_2 + y_1 y_2 + z_1 z_2 \tag{29}$$

for the scalar product (the flat Euclidean metric) of elements $q_i \in \mathbb{R}^3$, recall that we defined the two-sphere as all points q with $q \cdot q = \rho^2$. On this two-sphere, the flat metric (29) induces a constantly curved metric with curvature $+1/\rho^2$. All distance measurements, including those occurring during the Poisson disc sampling on the sphere, have to be done with respect to this nontrivial metric. Similarly, introducing the notation

$$q_1 * q_2 \equiv (x_1, y_1, z_1) * (x_2, y_2, z_2) = x_1 x_2 + y_1 y_2 - z_1 z_2 \tag{30}$$

for the indefinite scalar product (the flat three-dimensional Minkowski metric) for elements $q_i \in \mathbb{R}^3$, we define hyperbolic space as all points q for which $q * q = -\rho^2$ and $z > 0$. On this upper sheet of the two-dimensional hyperboloid, the metric (30) induces a constantly curved, positive definite metric with curvature $-1/\rho^2$. Again, this nontrivial metric must be used when measuring geodesic distances on the two-dimensional hyperbolic space.

Note that for a pair of points (p, q) on the two-sphere, given in terms of their Cartesian coordinates, their geodesic distance on the sphere can be expressed with the help of the scalar product (29) as

$$d(p, q) = \rho \arccos\left(\frac{p \cdot q}{\rho^2}\right). \tag{31}$$

In a similar fashion, the geodesic distance of two points (p, q) on hyperbolic space, given in terms of their Cartesian coordinates is

$$d(p,q) = \rho \operatorname{arccosh}\left(-\frac{p * q}{\rho^2}\right), \tag{32}$$

using the inner product (30). The minus sign in the argument of the inverse hyperbolic cosine comes from our choice of overall sign in the Minkowskian scalar product (30). Relevant for the construction of an annulus around some point p on the two-sphere – needed in the Poisson disc sampling – is the fact that the set of all points at a constant distance d from p *on the sphere* also forms a planar circle in the embedding space $\mathbb{R}^3$. This is made explicit by expressing the scalar product $p \cdot q$ in eq. (31) in terms of the *three*-dimensional Euclidean distance $d_{\mathrm{eu}}(p,q)$ of the two points, leading to

$$d_{\mathrm{eu}}(p,q) = 2\rho \sin\left(\frac{d(p,q)}{2\rho}\right). \tag{33}$$

This is an injective relation between d and d_{eu} as long as $d < \pi\rho$, a condition that in our applications was always satisfied.

When implementing the Poisson disc sampling on the sphere, after picking a point p to serve as the centre of an annulus, we parametrize the neighbourhood of p in terms of a two-dimensional system of radial coordinates (r, φ) centred at p, such that the inner and outer boundary of the annulus (at geodesic distances d_{min} and $2\,d_{\mathrm{min}}$) are circles of constant radius r. Like in the flat case, points in the annulus are then created randomly and uniformly, this time with respect to the appropriate measure on the two-sphere, expressed in terms of the variables r and φ. For each newly created point, we perform a test to make sure that its distance to all other points already included in the set P is larger than d_{min}. If this is the case, the point is added to the set, otherwise it is discarded. We did not attempt to set up suitable analogues of the square grid on the sphere or the hyperboloid to speed up this part of the algorithm, and instead simply computed the distance of a given candidate point to all other points. Since we considered only relatively small configurations with up to 20.000 points, the resulting increase in computational complexity to $O(n^2)$ could be handled without problems.

The Poisson disc sampling in the hyperbolic case proceeds along similar lines, the only minor difference being that the set of all points equidistant to a given point p on the hyperboloid do in general not lie on a circle with respect to the *Euclidean* metric of the embedding $\mathbb{R}^3$. To nevertheless be able to use a straightforward generalization of the procedure on flat space and the sphere, we boost the centre p of an annulus to the lowest point $(0, 0, \rho)$ of the hyperboloid, because in this case the set of all points equidistant to p does lie on a planar circle in the embedding space. We can again introduce a spherical coordinate system on a local, two-dimensional neighbourhood of p and implement the disc sampling as before, with respect to the induced, non-trivial measure on the hyperboloid. Once a candidate point has been chosen randomly from the annulus, it is boosted back, after which the usual distance check to all other points is performed with the help of eq. (32).

The next step consists in generating Delaunay triangulations from the point sets P we have constructed on the curved spaces using Poisson disc sampling, as described above. In the curved context, we again define a Delaunay triangulation through the property that any (geodesic) circumcircle of the triangulation built from P does not have any elements of P inside. This construction remains meaningful – in the sense of resembling the procedure in flat space – as long as the size of the triangles is small compared to the curvature radius of the constantly curved spaces we are considering, which was always the case.

The code we used to generate the triangulations is based on reference [18], which makes use of Voronoi diagrams (also called Voronoi or Dirichlet tessellations). Recall that the Voronoi diagram associated with a finite point set P, for simplicity taken to lie in the Euclidean plane, partitions the plane into cells. Each cell is associated with a point $p \in P$ and consists of all points in $\mathbb{R}^2$ that are closer to p than to any other point of P, so that each cell has the shape of a convex polygon. The set of all line segments forming the borders between adjacent cells forms a graph whose vertices are tri- or higher-valent. A generic point set, like the random sets P we construct with the help of the Poisson disc sampling, has a unique, trivalent "Voronoi graph" associated with it, which in turn is dual to the unique Delaunay triangulation constructed from the same point set. An analogous construction also goes through for the "mildly curved" spaces we are considering, with the Euclidean distance substituted by the appropriate geodesic distance on these spaces. Note that the vertices of the Voronoi diagram coincide with the centres of the circumcircles of the dual Delaunay triangulation.

The algorithm in [18] proceeds iteratively, adding in each step a vertex to an already existing Delaunay triangulation. Data are stored and manipulated referring to the vertices of the triangulation as well as to the (dual) vertices of the Voronoi diagram, which also means that the new elements of the latter have to be computed and updated in each step. The beauty of the set-up lies in the fact that these updates only affect small local neighbourhoods of the triangulation. We will not describe details of the algorithm here, which can be found in [18] for Euclidean spaces, but only describe the modifications that are necessary in the curved case.

Firstly, we need to choose an initial Delaunay triangulation. For the case of positive curvature, we pick four vertices on the sphere which span an equilateral tetrahedron in the embedding $\mathbb{R}^3$, and connect them by geodesic arcs on the sphere. Obviously, the length of these initial edges is much larger than $d_{\min}$, but they quickly disappear as the algorithm progresses, since it includes the creation and removal of links in each step. By contrast, for the case of negative curvature, since the upper sheet of the hyperboloid has infinite volume, we must impose a cutoff to make the construction well defined. Our prescription was to consider only points with embedding space coordinate $z \leq z_{\max} = 3\rho$. Just like in flat space, we therefore are dealing with a spatial region with a boundary. Vertices on the boundary $z = 3$ were again generated with a one-dimensional Poisson sampling of geodesic distances in the interval $[d_{\min}, 2\, d_{\min}]$. The initial triangulation of this hyperbolic disc is obtained by connecting each boundary vertex to the apex $(0, 0, \rho)$ of the hyperboloid by a geodesic line segment. The length of these segments exceeds $2\, d_{\min}$, but again this does not seem to leave any imprint on the final triangulations.

Secondly, we need an effective method to compute the locations of the vertices of the Voronoi diagram dual to a given Delaunay triangulation. More specifically, we must determine the centre of a circumcircle spanned by a triple of vertices of the triangulation, which requires a simple application of linear algebra. Put briefly, for both the sphere and the hyperboloid one first identifies the plane in $\mathbb{R}^3$ spanned by the difference vectors of the three vertices, using the cross product of vectors or a Gram-Schmidt procedure respectively. One then looks for the axis through the origin in $\mathbb{R}^3$ which is perpendicular to that plane, using the inner products (29) or (30) as appropriate, and finally determines the point in which the axis meets the sphere or the hyperboloid.

6.3 Measurement method

For all three types of geometry, the final step in constructing the triangulations that we will use for exploring our curvature prescription is to set all edge lengths of the Delaunay triangulations to unity. To give a quantitative impression of the distribution of edge lengths ℓ before making the triangulation equilateral, Fig. 12 shows a sample from a Delaunay triangulation of flat space. The edge lengths are distributed rather evenly across the interval $[d_{\min}, 2\, d_{\min}]$, increasing somewhat in the vicinity of $d_{\min}$, which by construction constitutes a kinematical lower bound, and decreasing towards longer lengths. The fact that very few edge lengths exceed $2\, d_{\min}$ reflects the well-behaved geometry of the triangulation.

Before embarking on the curvature measurements, we measured some other geometric properties of the triangulations to check whether they are roughly in line with those of the corresponding continuum geometries. For all three types of geometry, we measured the distribution of the vertex order[8], and also determined

---

[8] In two dimensions, the vertex order (the number of links meeting at a vertex) is a direct measure of the deficit angle and therefore of the local Gaussian curvature at a vertex.

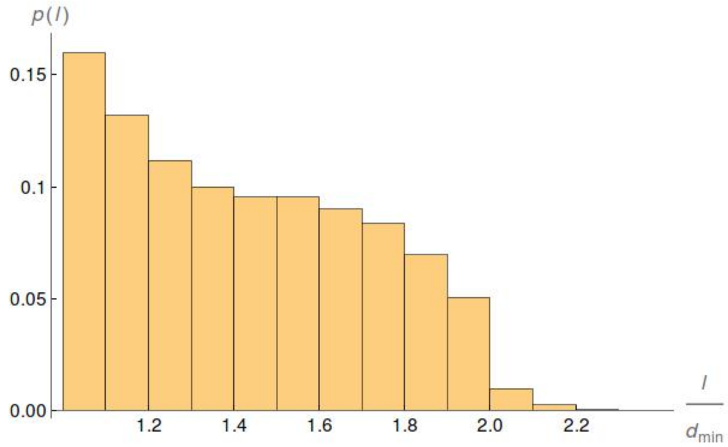

Figure 12: Probability distribution $p(\ell)$ of edge lengths ℓ in a Delaunay triangulation of flat space with 6.200 vertices, binned in intervals of 0.1 $d_{\min}$.

the scaling of the size of geodesic spheres (circles in our case) as function of their geodesic radius, and compared it to the corresponding continuum behaviour. For the spherical case, we also measured the distribution of diameters, where the diameter at a vertex is defined as the distance to the furthest vertex in the triangulation. By and large, these quantities behave as expected from a comparison with their continuum counterparts, as will be discussed below. This indicates that the configurations continue to be "nice" and compatible with an overall spatial uniformity also after removing the differences between length assignments from the Delaunay triangulations.

We then collected data on the average sphere distances $\bar{d}(S_p^\delta, S_{p'}^\delta)$ as a function of the geodesic (integer) link distance δ in the range $\delta \in [1, 15]$ for a given type of geometry (flat, spherical or hyperbolic), by averaging in each case over a set of ten independent triangulations, and over the location and relative orientation of pairs of spheres S_p^δ and $S_{p'}^\delta$.

For a given triangulated configuration, the latter averages were implemented as follows. After picking a vertex p in the triangulation, we constructed its δ-sphere S_p^δ, consisting of all vertices at link distance δ from p, and determined the total number of vertices in the sphere. For each of the vertices $p' \in S_p^\delta$ in turn, we then constructed a new δ-sphere $S_{p'}^\delta$ centred at p' and measured the average sphere distance $\bar{d}(S_p^\delta, S_{p'}^\delta)$. Averaging the resulting data over p' for given p implies an averaging over directions around p on the underlying space, thus removing directional information and producing an effective Ricci scalar curvature. Since we modelled our triangulations on isotropic continuum spaces, we expect them to be (approximately) isotropic too. Averaging over directions in this case is trivial and will just contribute to reducing numerical errors.

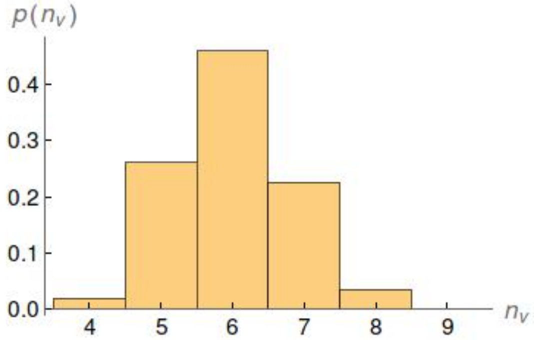

Figure 13: Distribution $p(n_v)$ of the vertex order n_v of interior vertices of a Delaunay triangulation of a piece of flat space with 6.200 vertices.

The way we picked a sequence of initial points p for a given configuration, for which the set of measurements just described was performed for all $\delta \leq 15$, was by simply using the first 20 points that were created during the Poisson disc sampling for this geometry. Recall that for the flat and hyperbolic spaces, which both have a boundary, we chose the initial point for the disc sampling to coincide with the centre of the space. Since points generated subsequently always lie within an annulus of a previously generated point, this implies that the first 20 points from such a sequence will be clustered not too far away from the centre. This was done mainly to avoid that the measurements run into the boundary of the triangulation.[9] It also means that our measurements will inevitably have some spatial overlap, and therefore not all data will be independent. However, since we also averaged over different configurations, we do not think that this procedure leads to any systematic errors.

6.4 Measurement results

Starting with the flat case, we investigated ten independent configurations, each with approximately 6.200 vertices. Fig. 13 shows the distribution of the order n_v of interior vertices of a sample triangulation. It is centred around 6, with more than 90% of vertices having coordination number 5, 6 or 7. The construction makes it impossible to have internal vertices of order smaller than 4, which explains why 4 is the lowest order observed. In the measurements considered we did not encounter vertices whose order was above 10. This is different from what happens in quantum configurations, like those appearing in dynamical triangulations, where the order distribution typically has a long tail at high vertex orders.

---

[9] We always made sure by additional checks that the minimal distance to the boundary of any point p was larger than 2δ.

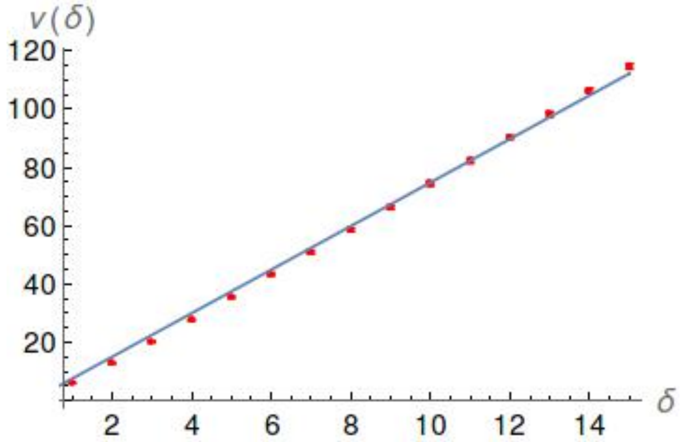

Figure 14: The (averaged) size $\nu(\delta)$ of circles as a function of their radius δ, on a geometry obtained by setting the edge lengths of a flat Delaunay triangulation to unity, including the best linear fit.

The absence of this feature for the Delaunay triangulations is another indicator of their well-behaved nature.

A first check of the flat character of the triangulations is a measurement of the scaling behaviour of geodesic circles, as explained in the previous subsection. We will denote the (discrete) volume of a circle of geodesic radius δ – equal to the number of vertices contained in the circle – by $\nu(\delta)$. A linear dependence on δ indicates flat-space behaviour, the corresponding relation in the continuum being $\nu(\delta) = 2\pi\delta$. In a context where distances are discretized because of the presence of building blocks of standard size, the proportionality constant on the right-hand side of this equation will typically not be equal to 2π, as is illustrated by the two-dimensional hexagonal lattice, one of the regular lattices we explored in Sec. 5, for which we have $\nu(\delta) = 6\delta$. This is a consequence of the lattice structure, where geodesic distances are not measured along straight lines in the conventional continuum sense, and where geodesic spheres are not smooth objects either. The data for the circle volume $\nu(\delta)$ collected from the ten configurations are displayed in Fig. 14, together with a best linear fit for the average circle volume, given by $\nu(\delta) = 7.48(5)\delta$. In the δ-range considered, the quality of the fit is good, showing that the behaviour is compatible with that of a flat space on scales sufficiently large relative to the lattice spacing.

Our measurements of the normalized average sphere distance $\bar{d}/\delta$ on the random triangulations at hand are shown in Fig. 15, where we have included the data for the regular hexagonal lattice and the constant continuum result for flat space for comparison. The behaviour of the random triangulation is qualitatively similar to that of the hexagonal lattice: for small $\delta \geq 1$, $\bar{d}/\delta$ has initially

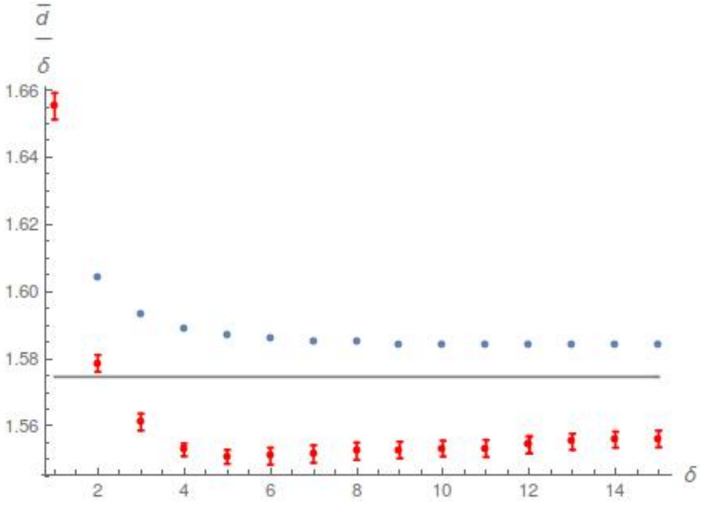

Figure 15: Normalized average sphere distance $\bar{d}/\delta$ as a function of the scale δ, measured on random triangulations modelled on flat space (red data points with error bars). For comparison, we have included the corresponding data for the flat hexagonal lattice (blue dots) of Fig. 9 and the horizontal line marking the constant value of continuum flat space (grey).

a maximum, then decreases, and for $\delta \gtrsim 5$ settles to an approximately constant value, consistent with flat-space behaviour. Unlike what we saw for the regular flat lattices, this value is now slightly below that for continuum flat space, and lies at approximately 1.55. The amplitude of the initial overshoot is in the same ballpark as those for the regular lattices (Fig. 8). From this point of view, any nontrivial curvature that is present in the random triangulation on short scales is mixed with and indistinguishable from the pure discretization effects of the flat lattices, as far as the quantum Ricci curvature is concerned.

To construct random triangulations modelled on non-flat spaces, we set without loss of generality the curvature radius of the underlying sphere and hyperboloid to one, $\rho = 1$. Choosing different values of d_{min} for the Poisson disc sampling then amounts to different degrees of fine-graining of the resulting triangulations with respect to this continuum reference scale. A smaller d_{min} corresponds to a finer-grained triangulation and therefore to a smaller value of the local curvature. After setting the edge lengths to 1, we expect to see these differences reflected in terms of lattice units. That is, we expect our measurements to be governed by an "effective curvature radius" ρ_{eff} in lattice units, which is inversely proportional to d_{min}. Moreover, by rescaling the results for random triangulations with different fine-grainings in such a way that their effective curvature radii coincide, we expect their measurement data to fall on top of each other.

We have studied the situation in considerable detail for the case of the sphere,

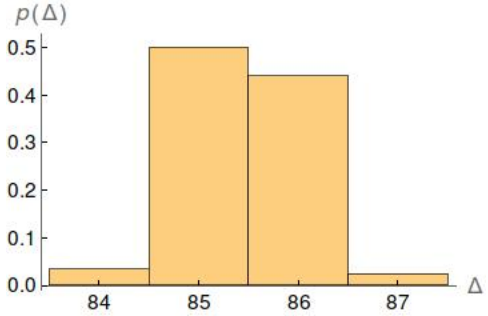

Figure 16: Distribution $p(\Delta)$ of diameters Δ of a sample spherical triangulation, generated using $d_{\mathrm{min}} = 0.025$.

where we have worked with three distinct continuum cutoffs, $d_{\mathrm{min}} = 0.1$, 0.05 and 0.025, and three different types of measurements from which an effective curvature radius can be extracted. Before embarking on these, we determined the vertex order distributions for the Delaunay triangulations of the sphere and found that for all three sizes considered they are almost indistinguishable from that of flat space depicted in Fig. 13.

We then measured the distribution of diameters Δ of the triangulations obtained after setting $\ell = 1$ for all edges, a quantity defined in subsection 6.3 above. In all cases the distributions are very narrow, further supporting the closeness of the configurations to round continuum spheres. An example is shown in Fig. 16 for a triangulation constructed with $d_{\mathrm{min}} = 0.025$. For $d_{\mathrm{min}}=0.1$, 0.05, 0.025, the average diameters (averaged over ten configurations) were measured to be $\Delta = 21.5(1)$, $42.9(1)$ and $85.5(1)$, which after division by π leads to the effective radii $\rho_{\mathrm{eff}} = 6.84(4)$, $13.65(3)$ and $27.22(3)$ respectively. Note that (within measuring accuracy) subsequent values differ by a factor of 2, as one would expect for consistency. As we will see below, these values are slightly, but systematically smaller (by about 7%) than those extracted from circle and curvature scaling, which do agree mutually. A possible explanation is that – unlike the latter quantities – the diameter by construction probes the largest scales of the lattices, and therefore is subject to systematic finite-size effects.

Next, we investigated the scaling of circle sizes $\nu(\delta)$ as a function of their geodesic radius δ, and compared them to the continuum formula $\nu(\delta) = 2\pi\rho\sin(\frac{\delta}{\rho})$. This gives us another way of extracting an effective curvature radius. However, in view of the analogous results for the flat case, we expect the overall factor to deviate from 2π. Furthermore, we have found that a (small) offset in δ improves the quality of the fits. The need for such a shift may have to do with the fact that for topological reasons (by virtue of the Gauss-Bonnet theorem for the two-sphere), the data is forced to go through the point $\nu(1) = 6$, resulting in a

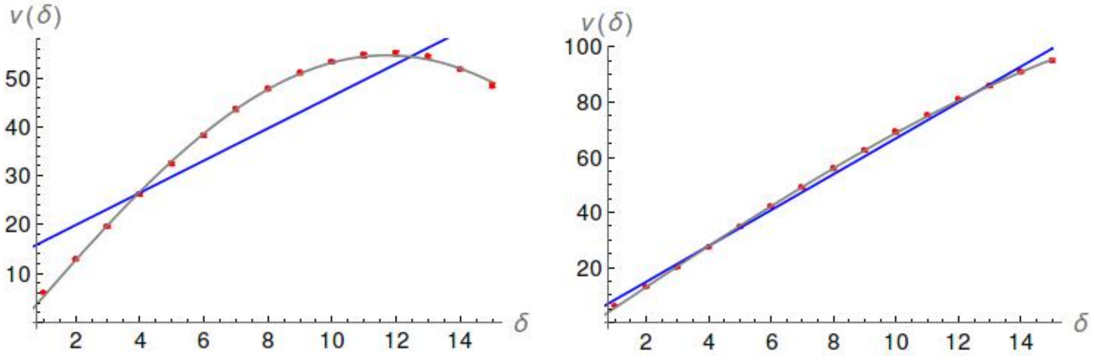

Figure 17: The (averaged) size $\nu(\delta)$ of circles as a function of their radius δ on spherical triangulations, for $d_{\text{min}} = 0.1$ (left) and $d_{\text{min}} = 0.05$ (right). We have included best fits to a function of the form $c\rho_{\text{eff}}\sin(\frac{\delta}{\rho_{\text{eff}}} + s)$ (grey curves), and to a linear function (blue curves).

distortion for small δ. The fitting function we have used is

$$\nu(\delta) = c\,\rho_{\text{eff}}\,\sin\left(\frac{\delta}{\rho_{\text{eff}}} + s\right), \tag{34}$$

for constants c and s. Fig. 17 illustrates the situation for the two larger values of d_{min}. In both cases, the sine function fits the data well. For comparison, we have also included linear fits to the data, but these are clearly inferior.

Obviously, within the limited range of δ-values we are exploring, it becomes more difficult to distinguish between flat and curved space as the (effective) curvature radius increases. This is illustrated by our last set of measurements, corresponding to $d_{\text{min}} = 0.025$, where within measuring accuracy the sine and linear functions fit the data about equally well. Not surprisingly, our estimate for the effective curvature radius has very large error bars. Table 1 summarizes the values for the constants s and c and the effective curvature radius ρ_{eff} obtained from best fits of $\nu(\delta)$, for the three different values of d_{min}.

The constant c is approximately constant, which is consistent with having a

d_{min}	s	c	ρ_{eff}
0.1	$-4.1(7)\cdot 10^{-2}$	7.5(1)	7.26(7)
0.05	$-1.9(3)\cdot 10^{-2}$	7.6(4)	15.6(5)
0.025	$-6(2)\cdot 10^{-3}$	7.4(23)	47(17)

Table 1: The parameters s, c and ρ_{eff} obtained from fitting circle sizes to the functional form $c\rho_{\text{eff}}\sin(\frac{\delta}{\rho_{\text{eff}}} + s)$, on spherical configurations of different sizes.

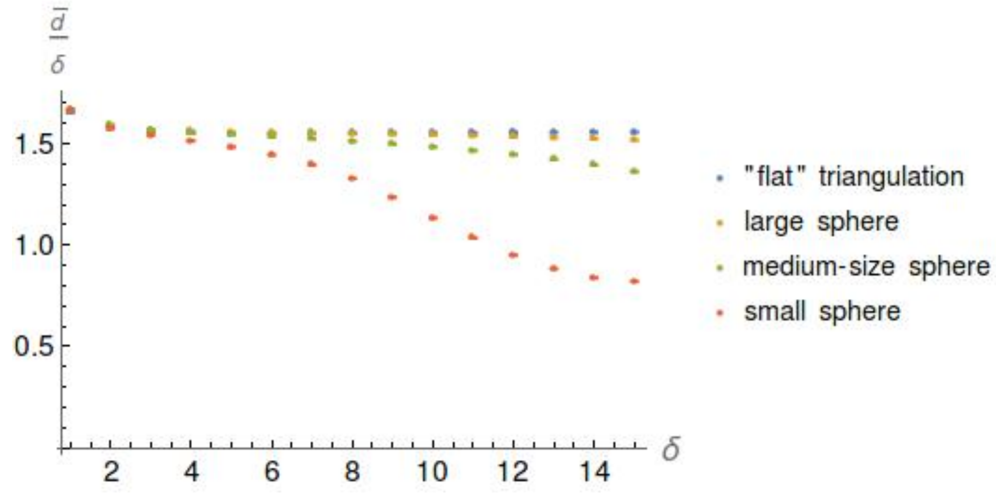

Figure 18: Normalized average sphere distance $\bar{d}/\delta$ as a function of the scale δ, measured on random triangulations modelled on continuum spheres of three different sizes. From top to bottom: "flat" random triangulation measured previously (for reference); large sphere ($d_{\min}=0.025$), medium-size sphere ($d_{\min}=0.05$), and small sphere ($d_{\min}=0.1$).

single, overall scale factor for the length of geodesic circles, compared to the continuum, independent of sphere size. The values lie within one standard deviation from the corresponding value 7.48(5) we found in the flat case.

Turning now to the measurements of the average sphere distance $\bar{d}(S_p^\delta, S_{p'}^\delta)$, Fig. 18 shows averaged values for the normalized quantity $\bar{d}/\delta$ for the three spherical triangulations, including the data for the flat random triangulation (from Fig. 15) for comparison. Qualitatively, the behaviour is as one would expect from the continuum: when moving to larger distances δ, the ratio $\bar{d}/\delta$ for the spheres goes to smaller values. The deviation from the horizontal flat-case line is largest for the smallest sphere, whose positive curvature is largest. For the largest sphere, the deviation from the flat case can be seen quite clearly for the largest measured values of δ, unlike the data from the circle scaling that did not allow us to distinguish between the two cases.

In order to make a quantitative comparison with the continuum, we would like to fit the data to curves of $\bar{d}/\delta$ for continuum spheres. However, we need to account for the observed difference in the constant c_q of eq. (7) between the continuum geometries on the one hand and regular lattices and triangulations modelled on constantly curved spaces on the other. This requires an additional rescaling of $\bar{d}/\delta$. There are two simple ways of achieving this, by applying either a multiplicative scaling or a constant, additive shift to $\bar{d}/\delta$. As we will see, both types of fit lead to similar results. To fix the additional matching parameter

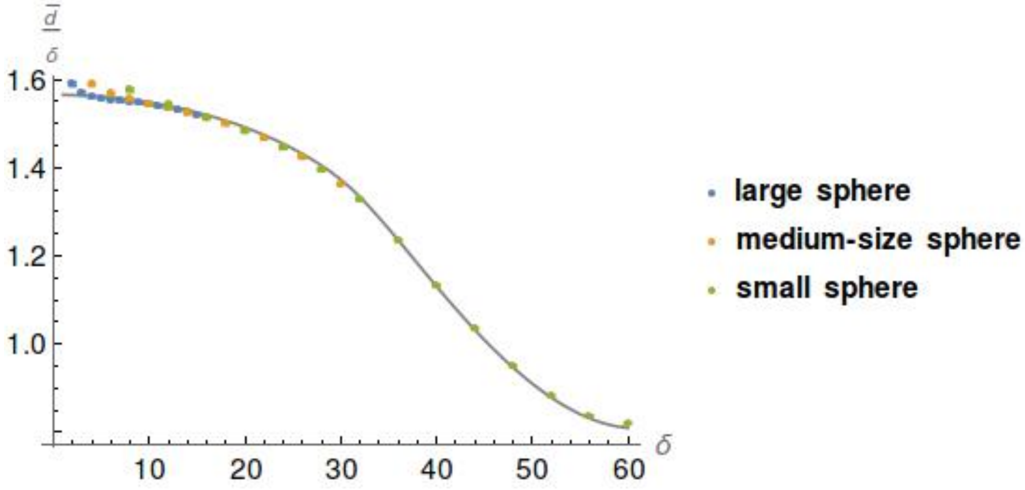

Figure 19: Measurements of $\bar{d}/\delta$ and best fit (using a multiplicative shift) to the corresponding data of a two-dimensional continuum sphere, for the combined and rescaled data of all three spheres. Error bars are smaller than dot sizes.

between continuum and discrete data, we require all curves to go through the data reference point at $\delta = 5$. It is natural to anchor the curves at this point, because it is the approximate location on the δ-axis where lattice artefacts seize to be significant.

In either case one is left with a one-parameter set of continuum curves, corresponding to different values of ρ. Among this set, we looked for the curve which best fitted our data, using a χ^2-fit for data points in the interval $\delta \in [6, 15]$. The smaller the sphere, the better is the quality of the fit.

The results for the effective curvature radius extracted from fitting to continuum spheres are collected in Table 2. We see that the two different types of fit lead to essentially identical results. Rescaling and combining the data for all three spherical configurations illustrates well that they can be fitted to a single contin-

d_{min}	ρ_{eff}, additive fit	ρ_{eff}, multiplicative fit
0.1	7.41(12)	7.35(9)
0.05	14.31(24)	14.27(21)
0.025	29.1(10)	29.0(13)

Table 2: Effective curvature radius ρ_{eff} of triangulations modelled on spheres, extracted from measuring the normalized average sphere distance, and fitting to continuum spheres, using an additive or multiplicative shift of the data, as described in the text.

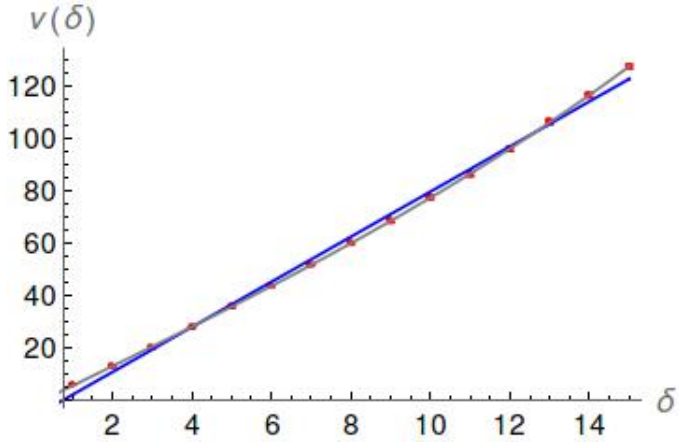

Figure 20: The (averaged) size $\nu(\delta)$ of circles as a function of their radius δ on geometries obtained by setting the edge lengths of Delaunay triangulations on a hyperboloid to unity, including best fits to a function of the form $\tilde{c}\rho_{\text{eff}}\sinh(\frac{\delta}{\rho_{\text{eff}}}+\tilde{s})$ (grey curve), and to a linear function (blue curve).

uum curve, modulo short-scale deviations (Fig. 19), supporting the existence of a universal underlying function $f(\delta/\rho)$.

To combine the data and obtain the joint curve, we first multiplied the δ-values of the data set for $d_{\text{min}} = 0.1$ by a factor 4, and that of $d_{\text{min}} = 0.05$ by a factor 2, bringing them to the linear scale of the largest sphere. The fit was obtained by considering the set of continuum curves going through the data point with $\delta = 5$ of the largest sphere and subsequently doing a χ^2-fit involving the 10 data points for the largest δ-values for each of the three spheres, i.e. a total of 30 data points. The curvature radius associated with the combined curve is $\rho = 29.0(3)$, corresponding to $\rho = 14.55$ for the medium-sized sphere and $\rho = 7.27$ for the small sphere, in very good agreement with the effective curvature radii we extracted from individual spheres and from measuring circle volumes. However, it is worth noting that obtaining the curvature radius from the prescription for quantum Ricci curvature for the same size of triangulation seems to give better results than obtaining it through circle scaling, despite the fact that the latter uses three instead of two fitting parameters.

Lastly, we report on the curvature analysis of the configurations obtained from the Delaunay triangulations on the two-dimensional hyperboloid. We performed measurements on ten independent configurations, which we constructed using $d_{\text{min}} = 0.04$. We had to restrict the δ-range to $\delta \leq 13$ to avoid coming too close to the boundary of the triangulations. The distribution of the interior vertex order resembles closely that of the flat and spherical cases. Next, we measured circle sizes $\nu(\delta)$ as a function of their radius δ. Following what we did in the spherical

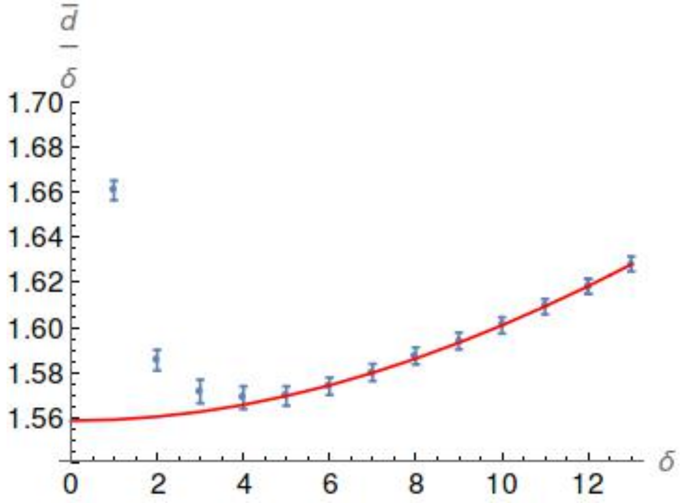

Figure 21: Normalized average sphere distance $\bar{d}/\delta$ as a function of the scale δ, measured on random triangulations modelled on a continuum hyperboloid (blue), shown together with a best fit of the corresponding curve in the continuum (red).

case, we used a three-parameter fit to extract an effective curvature radius ρ_{eff}. Substituting the sine by a hyperbolic sine function, we chose as a fitting function

$$\nu(\delta) = \tilde{c}\rho_{\text{eff}} \sinh\left(\frac{\delta}{\rho_{\text{eff}}} + \tilde{s}\right). \tag{35}$$

The continuum scaling would correspond to the special case $\nu(\delta) = 2\pi\rho\sinh(\frac{\delta}{\rho})$. From a best fit, we have determined the three parameters as $\tilde{s} = -1.69(17)\cdot 10^{-2}$, $\tilde{c} = 7.4(3)$ and $\rho_{\text{eff}} = 15.0(5)$. Like in the spherical case, the shift $\tilde{s}$ is small. The measured data are plotted in Fig. 20, together with the hyperbolic sine fit (35) and a linear fit through the origin for comparison. The former clearly fits the data better, providing further evidence that our triangulations approximate constantly curved continuum spaces also for negative curvature.

The measurements of the normalized average sphere distance for the hyperbolic case are shown in Fig. 21. We again performed two fits, a multiplicative and an additive rescaling of $\bar{d}/\delta$, combined with the requirement that curves should pass through the data point at $\delta = 5$. Both result in a very good match with the data; the best fit for the additive rescaling is displayed in Fig. 21. (It is barely distinguishable from the fit for multiplicative scaling.) As in previous measurements, there is a short-distance regime where $\bar{d}/\delta$ exhibits an "overshoot". From best matching for the data points $\delta \in [6, 13]$, we determined the effective curvature radius as $\rho_{\text{eff}} = 18.0(3)$ for the additive fit and $\rho_{\text{eff}} = 17.9(4)$ for the multiplicative fit. Both are in excellent agreement with each other, but not with the value we extracted from the circle scaling.

Comparing with the data for the smallest sphere, and using the fact that we expect the product $d_{\min} \cdot \rho_{\text{eff}}$ to be approximately constant, one would expect the effective curvature radius in the hyperbolic case to lie in the interval $[18.0, 18.5]$. While the data coming from measuring the quantum Ricci curvature are perfectly compatible with this estimate, the data from the circle scaling are off by six standard deviations. The only plausible explanation we have at this stage is that the hyperbolic case suffers from finite-size effects, due to the exponential growth of the volume with the radius, which for the volumes we are considering affect the circle scaling, but apparently not the average sphere distances. This question can be settled by going to larger lattices, which is beyond the scope of our present work. However, the encouraging message is that in comparison, the measurement of the quantum Ricci curvature again appears to be more robust.

7 Summary, conclusions and outlook

In this paper, we have defined a new way of quantifying the curvature properties of metric spaces in terms of "quantum Ricci curvature". Our starting point was the known observation that on smooth spaces the distance between two spheres in general differs from the distance between their centres in a way that depends on the Ricci curvature. Building on this observation, we constructed a curvature observable that is scalable and straightforward to compute, as we have demonstrated in many explicit examples. We defined the quantum Ricci curvature initially on purely classical, Riemannian manifolds, using a generalized notion of distance between spheres, based on averaging over both spheres. This replaces the transportation distance (sometimes also called Wasserstein distance) used in the Ollivier curvature [7, 8]. A main motivation was computability, especially in view of the fact that we want to evaluate the curvature also on large scales.

One could investigate the properties of quantum Ricci curvature in the classical continuum context in greater detail, but the prime aim of our current study was to show its feasibility in generalized, non-smooth settings, preparing the ground for its application in fully fledged quantum gravity. We limited our continuum analysis to the evaluation of the quantum Ricci curvature on two-dimensional spaces of constant curvature, which gave us a first quantitative grasp of the large-scale behaviour of this quantity. Note that on a two-dimensional Riemannian manifold the local Ricci curvature $Ric(v, v)$, for any vector v, coincides (up to a factor of 2) with the Ricci scalar.[10] The characteristic behaviour of the normalized average sphere distance for positive, zero and negative curvature shown in

---

[10] This is no longer true in higher dimensions, where the evaluation of the normalized average sphere distance for infinitesimal $\delta = \epsilon$ at order δ^3 yields a linear combination of the Ricci curvature and the Ricci scalar [15].

Fig. 6 also served as a benchmark for our subsequent curvature measurements on non-smooth spaces.

We described in Sec. 2 the challenge of defining a meaningful notion of curvature on non-smooth metric spaces, which in general lack a differentiable structure and the tensorial quantities that go with it. This raises the question of how a genuine tensor like the Ricci curvature $R(v,v)$ associated with a vector v can be represented. The analogue of a vector v of length δ in our implementation of the quantum Ricci curvature is given by a pair of overlapping spheres or balls of radius δ. When δ is an integer, like in the piecewise flat spaces we considered, the smallest value where the quantum Ricci curvature can be evaluated is $\delta = 1$, which is why we call it a "quasi-local" quantity.

Our analysis of the quantum Ricci curvature on piecewise flat spaces was motivated directly by the nonperturbative quantum theory formulated in terms of causal dynamical triangulations. As already emphasized in the introduction, the triangular building blocks in that case play the role of a short-distance regulator: the space of all D-dimensional spacetimes – the configuration space of the gravitational path integral – is approximated by a space of simplicial manifolds whose building blocks are equilateral D-simplices of some fixed edge length a. Since the details of the chosen regularization should not matter in the final continuum theory, physically interesting continuum limits $a \rightarrow 0$ should not depend on them at any scale, including the Planck scale. We discard measurements near the cut-off a as "discretization artefacts", because they usually bear a strong imprint of these details. In this respect our perspective on generalized Ricci curvature is different from that frequently taken in discrete mathematics and network theory, where the discrete, short-scale structure in itself is the primary focus of interest. This is also the case in recent implementations of Ricci curvature à la Ollivier in attempts to construct a theory of quantum gravity from specific statistical ensembles of random graphs or networks [19] (see also [20] for related ideas).

With the large-scale perspective in mind, we first studied the behaviour of the quantum Ricci curvature on regular flat lattices in two and three dimensions. These structures are "flat", in the sense that they can be imbedded in flat Euclidean space, from which they inherit their (unit) edge length assignments. We can treat these lattices as piecewise flat structures and work with the discrete geodesic link distance to compute lengths and geodesic spheres, thus providing a first test of the quantum Ricci curvature in a discretized setting.

All regular lattices we investigated display some common characteristics. They have a short-distance regime where the normalized average sphere distance $\bar{d}/\delta$ starts out at some maximum value for $\delta = 1$ and then decreases rapidly until about $\delta = 5$, where the $\bar{d}/\delta$-curve enters its flat regime. The presence (in our interpretation) of lattice artefacts below $\delta = 5$ means that we should not consider the limit $\delta \rightarrow 0$ to extract the constant c_q of relation (7), as we did in the continuum, but rather evaluate $\bar{d}/\delta$ at $\delta = 5$, or elsewhere in the constant region. Following this logic, we found that the value of c_q differs from the corresponding value in the smooth case, and also depends on the lattice type.

Since the regular lattices can be thought of as simple discretizations of flat space, one would expect them to behave like flat spaces in the continuum sense on scales that are sufficiently large in terms of lattice units. The corresponding lattice- and discretization-independent analogue of this behaviour appears to be the vanishing of the quantum Ricci curvature, $K_q = 0$ (or, equivalently, the constancy of the quantity $\bar{d}/\delta$), providing further justification for the ansatz (7).

The equilateral random triangulations we investigated next probe different properties of the quantum Ricci curvature. We constructed these triangulations with the intention of having them resemble constantly curved continuum spaces on large scales, while introducing random curvature fluctuations on small scales. It is not a foregone conclusion that the local small-scale curvature will "average out" on coarse-grained scales with respect to any measure of curvature, but this is exactly what we observed when evaluating the quantum Ricci curvature as a function of the scale δ.

For the triangulated spaces modelled on Delaunay triangulations of flat space, the results for the normalized average sphere distance resembled closely those of the regular flat lattices. Within measuring accuracy, the $\bar{d}/\delta$-curve is flat for distances $\delta \gtrsim 5$, signalling a vanishing of the quantum Ricci curvature. For smaller δ, applying formula (7), the quantum Ricci curvature is nominally negative, but since we have already identified this region as dominated by lattice artefacts, this statement has little physical significance. The same is true for the short-distance behaviour of the equilateral random triangulations modelled on Delaunay triangulations of curved spaces. The measurements of the normalized average sphere distances for $\delta \geq 5$ in these cases could be matched well to the corresponding continuum curves for spheres and hyperboloids. After performing a single shift in $\bar{d}/\delta$ to account for the a priori unknown c_q-value of a given type of piecewise flat space, we extracted effective curvature radii from a best matching to the continuum curves. All results were consistent with each other (e.g. for different sphere sizes) and consistent with the behaviour of the constantly curved continuum spaces they were meant to approximate in the first place. We also noted in passing that extracting the effective curvature radius from measuring the quantum Ricci curvature seems to give more accurate results than obtaining it from the scaling of sphere sizes.

To summarize, our analytical and numerical investigations of the novel quantum Ricci curvature on "nice" equilateral triangulations of moderate size, mostly in two dimensions, have demonstrated that it can be implemented and measured in a straightforward way. Lattice artefacts are confined to a scale of about five lattice spacings, above which the behaviour of the quantum Ricci curvature conforms with continuum expectations. In other words, away from the cutoff scale it is sensitive to neither lattice discretization effects nor the local curvature defects we introduced by removing the link length information from the Delaunay triangulations. In our view, the observed robustness of the quantum Ricci curvature has to do with the fact that the underlying normalized average sphere distance $\bar{d}/\delta$ is a dimensionless quotient of two quantities of the same kind, namely, an average distance and a distance, which will be affected by lattice discretization effects in a similar way.

These promising results pave the way for an evaluation of the quantum Ricci curvature on a nonperturbative quantum ensemble of spacetimes, like that of Causal Dynamical Triangulations. Of course, to obtain a proper quantum observable, we must perform a suitable average over spacetime points. This will then in turn be evaluated in the sense of eigenvalues, that is, by averaging over the spacetime configurations in the ensemble. Our implementation of quantum Ricci curvature in two-dimensional quantum gravity in terms of dynamical triangulations demonstrates that such a procedure is feasible and meaningful, even in a situation where the underlying geometric configurations are very far removed from smooth classical spaces [15]. The results obtained in this case further underline the robustness and good behaviour under averaging of the quantum Ricci curvature we found in the work presented here.

Acknowledgments

This work was partly supported by the research program “Quantum gravity and the search for quantum spacetime” of the Foundation for Fundamental Research on Matter (FOM, now defunct), financially supported by the Netherlands Organisation for Scientific Research (NWO). It was also supported in part by Perimeter Institute for Theoretical Physics. Research at Perimeter Institute is supported by the Government of Canada through Industry Canada and by the Province of Ontario through the Ministry of Economic Development and Innovation.

References

[1] J. Ambjørn, A. Görlich, J. Jurkiewicz and R. Loll, *Nonperturbative quantum gravity*, Phys. Rept. **519** (2012) 127-210 [arXiv:1203.3591, hep-th].

[2] J. Ambjørn, J. Jurkiewicz and R. Loll, *Spectral dimension of the universe*, Phys. Rev. Lett. **95** (2005) 171301 [hep-th/0505113].

[3] M. Reuter and F. Saueressig, *Fractal space-times under the microscope: A renormalization group view on Monte Carlo data*, JHEP **1112** (2011) 012 [arXiv:1110.5224, hep-th].

[4] S. Carlip, *Spontaneous dimensional reduction in quantum gravity*, Int. J. Mod. Phys. D25 (2016) 1643003 [arXiv:1605.05694, gr-qc].

[5] J. Ambjørn, J. Jurkiewicz and R. Loll, *Reconstructing the universe*, Phys. Rev. D **72** (2005) 064014 [hep-th/0505154];
J. Ambjørn, A. Görlich, J. Jurkiewicz, R. Loll, J. Gizbert-Studnicki and T. Trzesniewski, *The semiclassical limit of Causal Dynamical Triangulations*, Nucl. Phys. B **849** (2011) 144-165 [arXiv:1102.3929, hep-th].

[6] A. Platania and F. Saueressig, *Functional renormalization group flows on Friedman-Lemaitre-Robertson-Walker backgrounds* [arXiv:1710.01972]

[7] Y. Ollivier, *Ricci curvature of Markov chains on metric spaces*, J. Funct. Anal. 256 (2009) 810-864.

[8] Y. Ollivier, *A survey of Ricci curvature for metric spaces and Markov chains*, in Probabilistic approach to geometry, Adv. Stud. Pure Math., Math. Soc. Japan 57 (2010) 343-381.

[9] T. Regge, *General relativity without coordinates,* Nuovo Cim. **19** (1961) 558.

[10] R. Loll, *Discrete approaches to quantum gravity in four-dimensions*, Living Rev. Rel. **1** (1998) 13 [gr-qc/9805049].

[11] H.W. Hamber and R.M. Williams, *Simplicial quantum gravity with higher derivative terms: Formalism and numerical results in four-dimensions*, Nucl. Phys. B **269** (1986) 712-743.

[12] L. Brewin, *The Riemann and extrinsic curvature tensors in the Regge calculus*, Class. Quant. Grav. **5** (1988) 11931203.

[13] P.M. Alsing, J.R. McDonald and W.A. Miller, *The simplicial Ricci tensor*, Class. Quant. Grav. **28** (2011) 155007 [arXiv:1107.2458, gr-qc].

[14] J. Ambjørn, A. Görlich, J. Jurkiewicz and R. Loll, *Wilson loops in nonperturbative quantum gravity*, Phys. Rev. D **92** (2015) no.2, 024013 [arXiv:1504.01065, gr-qc].

[15] N. Klitgaard and R. Loll, Quantizing quantum Ricci curvature, to appear.

[16] B. Loisel and P. Romon, *Ricci curvature on polyhedral surfaces via optimal transportation*, Axioms 3 (2014) 119-139 [arXiv:1402.0644, math.DG].

[17] J. Guo, D.M. Yan, G. Bao, W. Dong, X. Zhang and P. Wonka, *Efficient triangulation of Poisson-disk sampled point sets*, Visual Computer 30 (2014) 773-785.

[18] A. Bowyer, *Computing Dirichlet tessellations*, Comput. J. 24 (1981) 162-166.

[19] C.A. Trugenberger, *Random holographic "large worlds" with emergent dimensions*, Phys. Rev. E **94** (2016) no.5, 052305 [arXiv:1610.05339, cond-mat.stat-mech]; *Combinatorial quantum gravity: geometry from random bits*, JHEP **1709** (2017) 045 [arXiv:1610.05934, hep-th].

[20] Z. Wu, G. Menichetti, C. Rahmede and G. Bianconi, *Emergent complex network geometry*, Sci. Rep. 5 (2015) 10073;
G. Bianconi and C. Rahmede, *Network geometry with flavor: from complexity to quantum geometry*, Phys. Rev. E **93** (2016) no.3, 032315 [arXiv:1511.04539, cond-mat.stat-mech].